

# Biomedical Visualization

Chris R. Johnson and Xavier Tricoche

*Scientific Computing and Imaging Institute*

*University of Utah*

*Salt Lake City, UT 84112, USA*

*www.sci.utah.edu*

---

## Abstract

*Key words:* , Biomedical Visualization, Scalar Field Visualization, Vector Field Visualization, Tensor Field Visualization, Uncertainty Visualization, Visualization Software

*PACS:*

---

## 1 Introduction

Computers are now extensively used throughout science, engineering, and medicine. Advances in computational geometric modeling, imaging, and simulation allow researchers to build and test models of increasing complexity and thus to generate unprecedented amounts of data. As noted in the NIH-NSF Visualization Research Challenges report [1], to effectively understand and make use of the vast amounts of information being produced is one of the greatest scientific challenges of the 21st Century. Visualization, namely helping researchers explore measured or simulated data to gain insight into structures and relationships within the data, will be critical in achieving this goal and is fundamental to understanding models of complex phenomena. In this chapter, we give an overview of recent research in visualization as applied to biomedical applications, focusing on the work by researchers at the Scientific Computing and Imaging (SCI) Institute [2].

Schroeder, Martin, and Lorensen have offered the following useful definition of visualization [3]:

Scientific visualization is the formal name given to the field in computer science that encompasses user interface, data representation and processing algorithms, visual representations, and other sensory presentation such as

sound or touch. The term data visualization is another phrase to describe visualization. Data visualization is generally interpreted to be more general than scientific visualization, since it implies treatment of data sources beyond the sciences and engineering.... Another recently emerging term is information visualization. This field endeavors to visualize abstract information such as hyper-text documents on the World Wide Web, directory/file structures on a computer, or abstract data structures.

The field of visualization is focused on creating images that convey salient information about underlying data and processes. In the past three decades, there has been unprecedented growth in computational and acquisition technologies, a growth that has resulted in an increased ability both to sense the physical world in precise detail and to model and simulate complex physical phenomena. As such, visualization plays a crucial role in our ability to comprehend such large and complex data – data which, in two, three, or more dimensions, convey insight into such diverse biomedical applications as understanding the bioelectric currents within the heart, characterizing white matter tracts by diffusion tensor imaging, and understanding morphology differences between different genetic mice phenotypes, among many others.



Fig. 1. The Visualization Pipeline.

Shown in Figure 1, the “visualization pipeline” is one method of describing the process of visualization. The *filtering* step in the pipeline involves processing raw data and includes operations such as resampling, compression, and other image processing algorithms such as feature-preserving noise suppression. In what can be considered the core of the visualization process, the *mapping* stage transforms the pre-processed filtered data into geometric primitives along with additional visual attributes, such as color or opacity, determining the visual representation of the data. *Rendering* utilizes computer graphics techniques to generate the final image using the geometric primitives from the mapping process.

While the range of different biomedical visualization applications is vast, the scientific visualization research community has found it useful to characterize scientific visualization techniques using a taxonomy associated with the dimensionality of the (bio)physical field to visualize:

- Scalar fields (temperature, voltage, density, magnitudes of vector fields, most image data),
- Vector fields (pressure, velocity, electric field, magnetic field), and
- Tensor fields (diffusion, electrical and thermal conductivity, stress, strain, diffusion tensor image data).

We use this taxonomy to discuss the biomedical visualization techniques throughout this chapter.

## 2 Scalar Field Visualization

Scalar data is prevalent in biomedical simulation and imaging. In biomedical computing, scalar fields represent a quantity associated with a single (scalar) number, such as voltage, temperature, the magnitude of velocity, *etc.* Scalar fields are among the most common datasets in scientific visualization, and thus they have received the most research attention (see [4] for an overview of scalar field visualization research). Biomedical scalar data, whether derived from simulations or gathered experimentally, often have both spatial and temporal components. These components have traditionally been visualized through different software structures. However, handling both spatial and temporal components of data within a single, unified software structure is not only convenient but will tend to strengthen the underlying visualization software by providing the *same* results whether the data is measured or computed.

### 2.1 Direct volume rendering

Direct volume rendering is a method of displaying three-dimensional volumetric scalar data as two-dimensional images and is probably one of the simplest ways to visualize volume data. The individual values in the dataset are made visible by the choice of a transfer function that maps the data to optical properties, like color and opacity, which are then projected and composited to form an image. As a tool for scientific visualization, the appeal of direct volume rendering is that no intermediate geometric information need be calculated, so the process maps from the dataset “directly” to an image. This is in contrast to other rendering techniques such as isosurfacing or segmentation, in which one must first extract elements from the data before rendering them. To create an effective visualization with direct volume rendering, the researcher must find the right transfer function to highlight regions and features of interest.

A common visualization goal in volume rendering is the depiction of the interface between two different materials in a volume dataset. The material surface can usually be seen with a simple transfer function which assigns opacity only to a narrow range of values between the data values associated with each of the two materials. In datasets characterized by noise or a more complicated relationship among multiple materials, statistical analysis of the dataset values can help to guide the transfer function design process. Moreover, in cases where datasets and associated volume rendering methods are more complex

(such as volumetric fields of vector or tensor values), methods for guiding the user toward useful parameter settings, based on information about the goals of the visualization, become necessary to generate informative scientific visualizations. Figure 2 shows a maximum intensity projection (MIP) of MRA data of the cerebral vasculature. The maximum intensity projection volume rendering method is the most simple form of volume rendering and is the one most often used by radiologists for viewing volume image data.



Fig. 2. A maximum intensity volume rendering of magnetic resonance angiography (MRA) data showing a large fusiform aneurysm.

The MIP algorithm works by projecting parallel rays (ray casting) through the volume from the viewpoint of the user. For each ray, the algorithm selects the maximum scalar value and uses that value to determine the color of the corresponding pixel on the two-dimensional image plane. Volume rendering using MIP yields what look like “three-dimensional x-rays” in gray scales of

the scalar volume data. Full volume rendering, on the other hand, traverses the rays and accumulates (integrates) color and opacity contributions along the ray. Volume rendering using full volume rendering techniques yields an image that looks much more like what you might expect a three-dimensional volume projection to look like in color. The differences are evident as shown below in Figure 3.

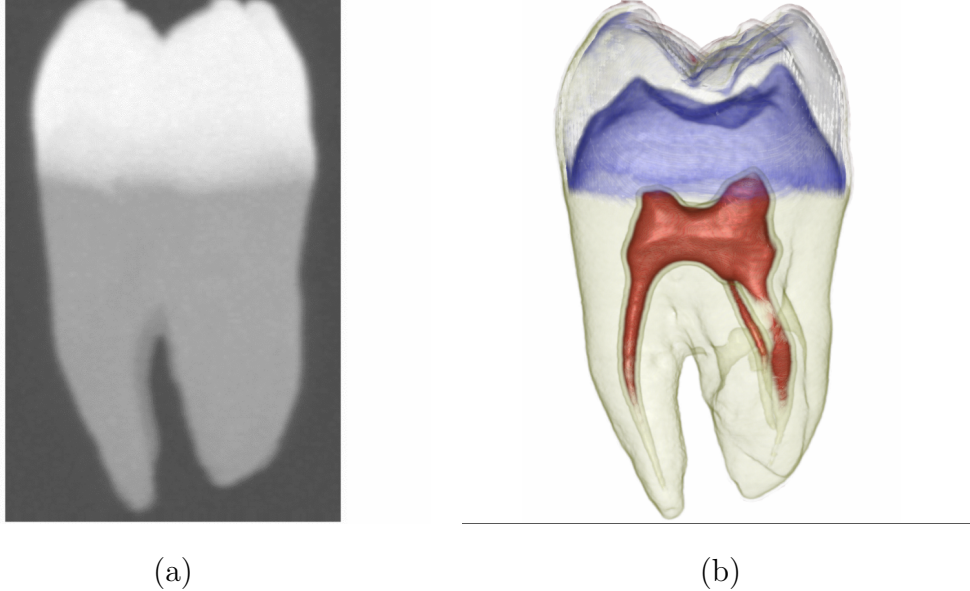


Fig. 3. (a) Maximum intensity projection (MIP) volume rendering of a tooth from CT data, and (b) a full volume rendering of the same data using multi-dimensional transfer functions with SCIRun (section 7.1).

The full volume-rendered image contains more information than the MIP-rendered image and is usually more useful for understanding the three-dimensional volume data or image. If this is true, why do most biomedical scientists use MIP and not full volume rendering? The answer is twofold. First, the MIP algorithm, since it only uses one value per voxel, is much less costly to compute than full volume rendering, which requires several values per voxel. This was the case especially before 2003, when graphics cards were not sufficiently powerful to generate fast full volume renderings. Second, full volume rendering is more difficult than the MIP algorithm to use. In particular, researchers find it difficult to relate the so-called transfer function to the scalar data values. This difficulty arose because most full volume rendering was originally done using one-dimensional transfer functions that involved manipulating the transfer function as a sort of ramp function, as shown in Figure 4. The method provided no intuitive way to choose the transfer function that might enable the user to see a particular feature in the data volume.



Fig. 4. Traditional one-dimensional ramp transfer function.

In some cases, volume visualization is more intimately tied to the imaging process. For instance, in electron microscope tomography (EMT) the configurations of the sample and electron beam limit the range of angles for which projections (*i.e.*, the sinogram) are acquired. This creates reconstruction artifacts that adversely affect the quality of virtually any direct rendering or visualization strategy. By using volume rendering to fit a surface to the data[5], we are able to estimate missing parts of the sinogram and create better three-dimensional reconstructions.

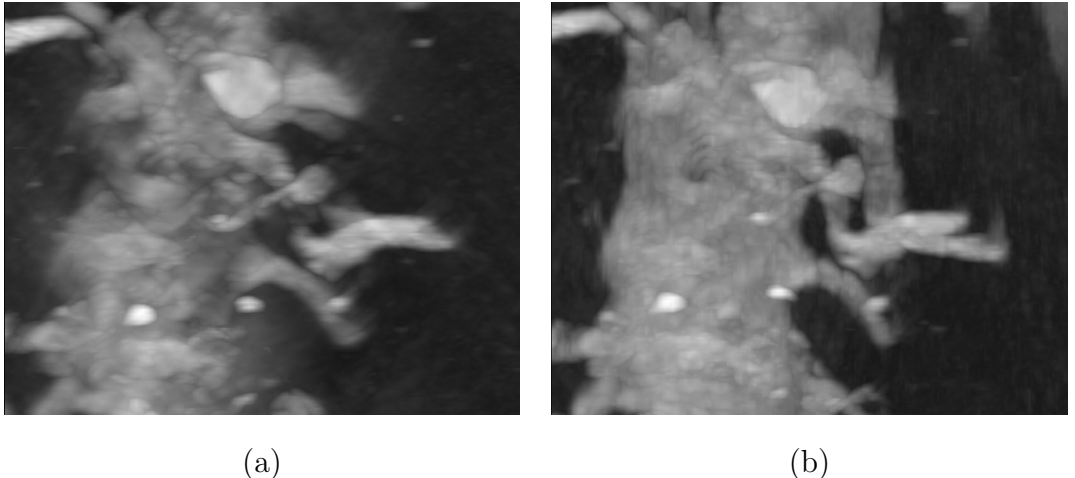


Fig. 5. Maximum intensity projection (MIP) renderings of electron microscope tomography volumes: (a) an image based on the raw data that exhibits reconstruction artifacts obfuscating the boundaries of this spiny dendrite, and (b) an image based on a data set that includes estimates of the missing views which reveals a more coherent picture of the structure.

Finding a good transfer function is critical to producing an informative rendering, but this is a difficult task even if the only variable to set is opacity. Looking through slices of the volume dataset allows the researcher to spatially locate features of interest, and the researcher may employ a means of reading off data values from a user-specified point on the slice to help in setting an opacity function to highlight those features. However, there is no way for the researcher to know how representative of the whole three-dimensional feature these individually sampled values are. User interfaces for opacity function specification typically allow the user to alter the opacity function by directly editing its graph, usually as a series of linear ramps joining adjustable control points. This interface does not itself guide the user toward a useful setting, as the movement of the control points is unconstrained and unrelated to the underlying data. Thus, finding a good opacity function tends to be a slow and frustrating trial-and-error process, in which apparently minor changes in an opacity function may lead to drastic changes in the rendered image. When the interaction of other rendering parameters, such as shading, lighting, and viewing angle, enters the picture, the process becomes even more confusing.

SCI Institute researchers have done substantial new research in volume rendering [6–15]. For example, Kindlmann and Kniss [15] have recently developed a method for the semi-automatic generation of transfer functions. In this method, the researcher creates a data structure, which we call the “histogram volume structure,” that captures information about the boundaries present in the volume and facilitates a high-level interface-to-opacity function creation. The user can determine which portions of the boundary will be made opaque without knowing the data values that occur in the boundary. Figure 6 illustrates an approach we have developed that is “semi-automated” in that it usefully constrains the user to a subspace of all possible transfer function while still allowing flexible depiction of surface features and characteristics[15].

Multi-dimensional transfer functions are sensitive to more than one aspect of the volume data, including, for example, both the intensity and one or more spatial gradients or other derived parameters. Such transfer functions have wide applicability in volume rendering for biomedical imaging and visualization. Even scalar datasets can benefit from multi-dimensional transfer functions. By incorporating edge-detection measures such as the first- and second-order spatial derivatives, we can easily discriminate between data values that represent material boundaries and those that represent the materials themselves. For instance, in a volume visualization of the Visible Male using CT data with the gradient magnitude and the second directional derivative in the gradient direction, we can accurately identify (classify) the sinuses, as seen in the right-hand panel of Figure 7. A method that uses only the CT data as the sole domain variable in a one-dimensional transfer function (shown in the left-hand panel of Figure 7 cannot produce a visualization with the same specificity[6].

Multi-dimensional transfer functions are also valuable for more general cases in which the data comes from multiple variables in a physical simulation or multiple medical imaging modalities. In such a case, the transfer function allows one to identify phenomena or features that can be described or classified based only on the basis of unique combinations of data values. Medical imaging can also benefit from multi-dimensional transfer functions when features of interest are not adequately described by any one imaging modality. For instance, CT imaging captures variations in bone structure but does not differentiate soft tissues well, whereas MR imaging differentiates soft tissue well and bone very poorly. By visualizing a co-registered CT and MRI dataset simultaneously, one can visualize features of interest in the soft tissue along with important bone landmarks.

To resolve the complexities inherent in a user interface for multi-dimensional transfer functions, we introduced a set of direct manipulation widgets that make finding and experimenting with transfer functions an intuitive, efficient, and informative process. To achieve interactive response, we exploited

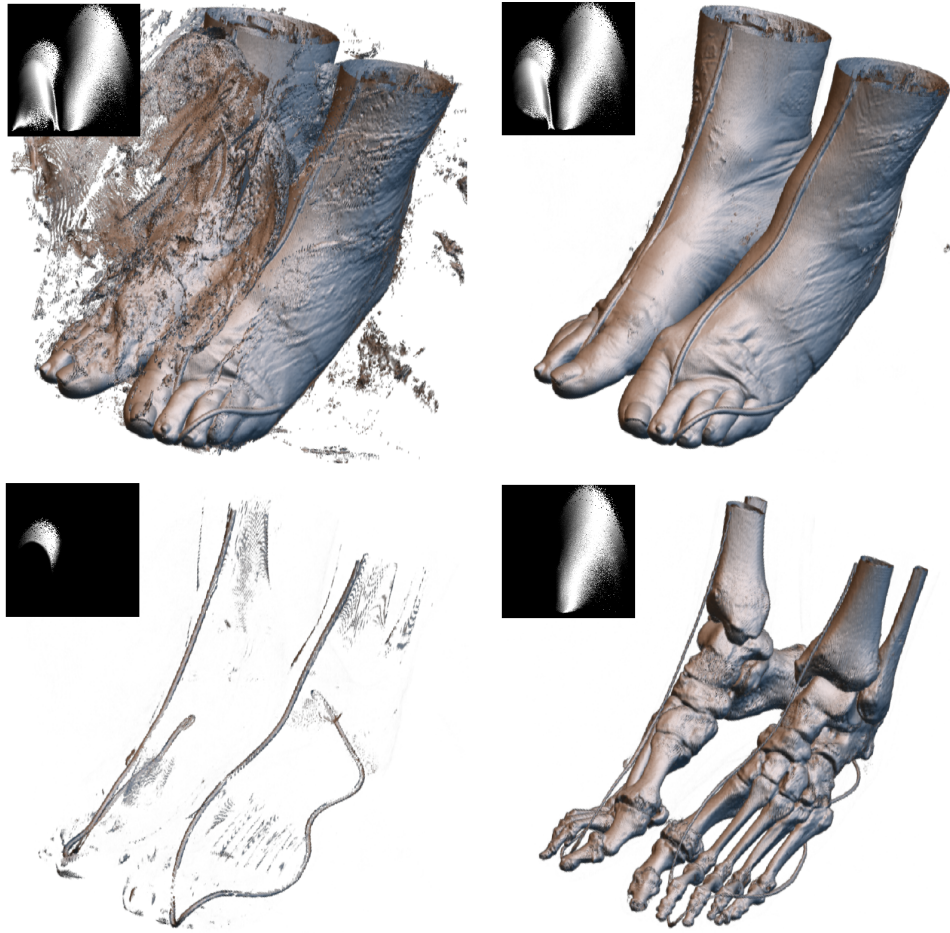


Fig. 6. Exploration of a CT dataset (Visible Human project, feet of the visible woman) with semi-automatically generated multi-dimensional transfer functions. The inset black-and-white images show the opacity assignment as a function of CT data value (horizontal axis) and gradient magnitude. The image in the upper left was created through the use of default settings in the semi-automatic method. A researcher familiar with the data can identify the obscuring structures as being associated with the bag in which the specimen was placed prior to freezing and scanning. When the corresponding region is eliminated from the transfer function domain (upper right), the skin structure is clearly visible. The remaining features in the transfer function domain can be identified as the surface of the registration cord (lower left) and the bone surface (lower right). Such specificity is not possible with standard one-dimensional transfer functions.

the fast rendering capabilities of modern graphics hardware, especially three-dimensional texture memory and pixel texturing operations. Together, the widgets and the hardware form the basis for new interaction modes that guide the user toward transfer function settings appropriate for their visualization and data exploration interests [16,10,17].

The generalization of direct volume rendering to multi-valued fields presents at least two research challenges on which future work can focus, the first in-

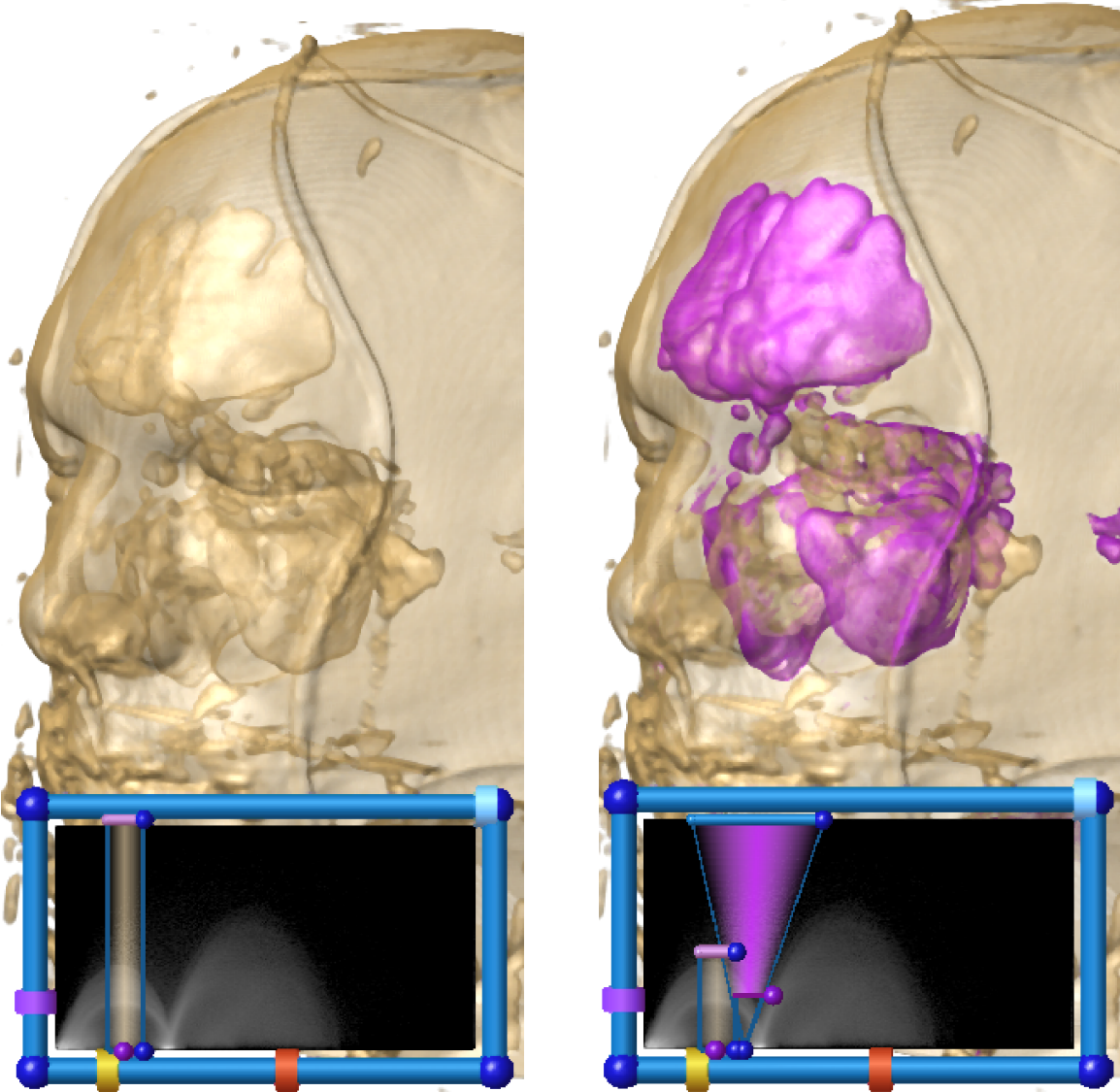


Fig. 7. A comparison of scalar (left) and multi-field (right) volume renderings of the Visible Male CT data.

volving surface shading and the second involving the efficient evaluation of multi-dimensional transfer functions. Crucial to successful volume rendering is the calculation from the original data of the spatial gradients with which shading and surface rendering will be performed. In scalar data, the gradient has a simple mathematical definition and computation. In multi-valued fields, however, the generalization of the gradient is matrix-valued, and the surface orientation is represented as an eigenvector of this matrix. Current volume rendering methods make little use this information because it is computationally expensive, although advances in the abilities of GPUs increasingly support these calculations at interactive rates.

As described above, multi-dimensional transfer functions permit the visual-

ization of structure based on combinations of values within the constituent fields. As the number of fields increases, simple implementations of multi-dimensional transfer functions become unwieldy. This observation motivated us to investigate analytic expressions for transfer function representation [7]. We have introduced a flexible framework for classifying and rendering multi-field datasets using transfer functions based on Gaussian primitives. We show in the paper that Gaussian transfer functions have a number of key features: they allow for selective classification of narrow features, can be efficiently computed on the graphics hardware, and their integral along a line segment has, under very limited assumptions, a closed-form analytic solution. Hence, they obviate the need for large precomputed lookup tables and are very memory efficient.

We expect this approach to have a large impact on the qualitative and quantitative value of volume rendering and become a significant tool for biomedical researchers. An example is shown in Figure 8.

**Example volume rendering applications** The power of volume rendering for the interactive investigation of complex medical datasets was demonstrated in the BioPSE software system with the BioImage PowerApp[18], developed at the SCI Institute. As an example of BioImage’s utility, we have used BioImage’s volume rendering tools to investigate the angiogenesis surrounding tumors in transgenic mice, as shown in Figure 9. The mouse vasculature, so clearly visible in this three-dimensional volume rendering, could only be clearly visualized using a tool with the powerful specificity of multi-dimensional transfer functions. In addition, the BioImage tool that provides the interactive rendering also allows the user to crop and filter their data; it allows the user to simultaneously view slices and volume renderings of their data; and it provides the user with a set of quantitative tools for directly probing values within his data.

The same volume rendering techniques can be used to on thoracic CT datasets to investigate lung tumors, as shown in Figure 10. With the BioImage volume rendering tools we can interactively explore the size and shape of lung tumors without compromising the fidelity of the original high-resolution CT data.

## 2.2 Isosurface extraction

Isosurface extraction is a powerful tool for investigating volumetric scalar fields. An isosurface in a scalar volume is a surface on which the data value is constant, separating regions of higher and lower value. Given the physical or biological significance of the data value (*i.e.*, radio-opacity, dye concentration,



Fig. 8. Example of 4D multi-field volume classified using a gaussian transfer function. The dataset is the Visible Male Color Cryosection, courtesy of the NLM NIH. The analytical integration of the transfer function along rays creates a high-quality representation. In particular muscles and boundaries between white and gray matter can be precisely isolated. Image courtesy of Joe Kniss [7]

fluorescence level), the position of an isosurface, as well as its relation to other neighboring isosurfaces, can provide clues to the underlying structure of the scalar field. In biomedical imaging applications, isosurfaces permit the extraction of particular anatomical structures and tissues; however, these isosurfaces are typically static in nature. A more dynamic use of isosurfaces can provide better visualization of complex space- or time-dependent behaviors in many scientific applications.

Within the last 15 years, isosurface extraction methods have advanced significantly, from an off-line, single-surface extraction process into an interactive, exploratory visualization tool. Interactivity is especially important in

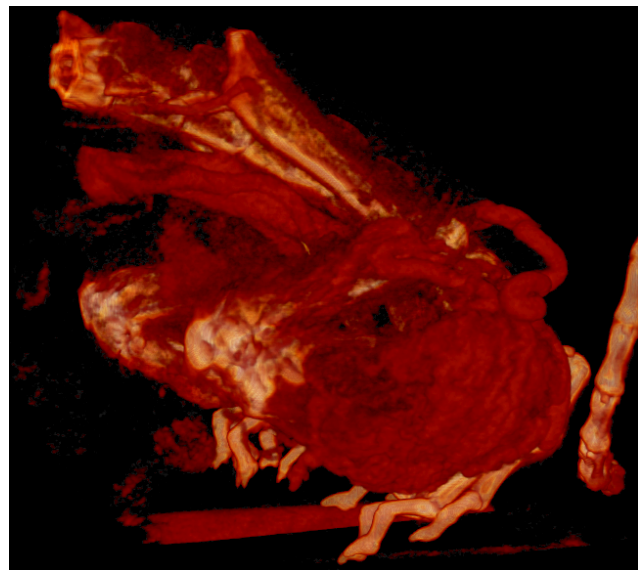


Fig. 9. Mouse data visualized with BioImage's multi-dimensional transfer function volume rendering. Data courtesy of Charles Keller.

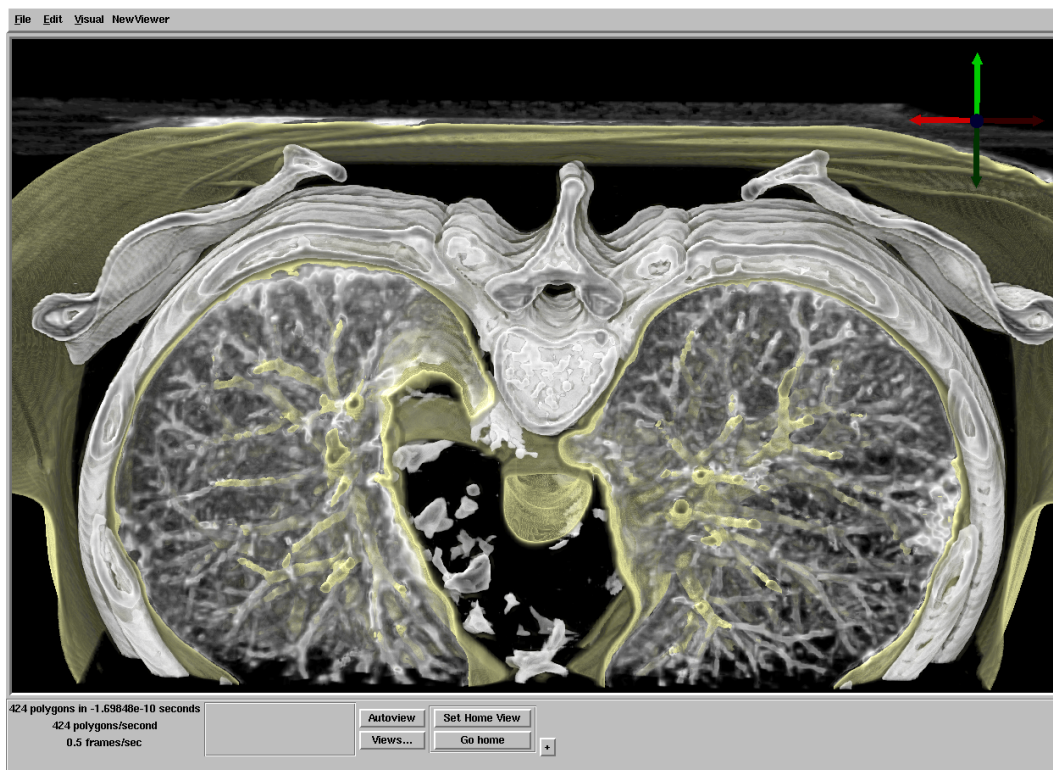


Fig. 10. A volume rendered image using multi-dimensional transfer functions. This view highlights the detailed vasculature of the lungs. Data courtesy of George Chen, MGH.

exploratory visualization where the user has no *a priori* knowledge of any underlying structures in the data. A typical data exploration session therefore requires the researcher to make many isovalue changes in search of interesting

features. In addition, it is helpful to provide global views (to place an isosurface in the context of the entire dataset) and detailed views of small sections of interest. Maintaining interactivity while meeting these visualization goals is especially challenging for large datasets and complex isosurface geometry.

The *Marching Cubes* [19,20] method, introduced in 1986, was the first practical and most successful isosurface extraction algorithm. Its simplicity has made it the *de facto* standard extraction method even to this date. The Marching Cubes algorithm demonstrated that isosurface extraction can be reduced, using a divide and conquer approach, to solving a local triangulation problem. In addition, the marching cubes method proposed a simple and efficient local triangulation scheme that uses a lookup table. Subsequently, researchers created methods for accelerating the search phase for isosurface extraction [21–25] all of which have a complexity of  $O(n)$ , where  $n$  is the number of voxels in the volume. We introduced the *span space* [26] as a means for mapping the search onto a two-dimensional space and then used it to create a *near optimal isosurface extraction* (NOISE) algorithm that has a time complexity of  $O(\sqrt{n} + k)$ , where  $k$  is the size of the isosurface. Cignoni et al. [27] employed another decomposition of the span space leading to a search method with optimal time complexity of  $O(\log n + k)$ , albeit with larger storage requirements. In addition, Bajaj et al. introduced the contour spectrum, which provides a fast isosurface algorithm and a user interface component that improves qualitative user interaction and provides real-time exact quantification in the visualization of isocontours [28,29].

We improved further on these isosurface extraction methods by using a different visibility testing approach and virtual buffer rendering to achieve a real-time, view-dependent isosurface extraction [30–33]. We also presented a progressive hardware assisted isosurface extraction (PHASE) that is suitable for remote visualization *i.e.*, when the data and display device reside on separate computers. This approach works by reusing, when a view point is changed, the information and triangles that were extracted from the previous view point [32]. Using this approach, we can extract only newly visible sections of the isosurface and thus improve visualization performance.

Following the same view-dependent approach we have recently proposed a novel point-based approach to isosurface extraction [33]. The basic idea of our method is to address the challenge posed by the geometric complexity of very large isosurfaces by a point-based representation of sub-pixel triangles. Combined with a new fast visibility query and a robust normal estimation scheme, our method allows for the interactive interrogation of large data sets (e.g. the full NIH NLM Visible Female dataset (1GB)) at up to 15 frames per second on a single desktop computer. We also presented an extension of that algorithm that enhances the isosurface visualization by computing shadows.

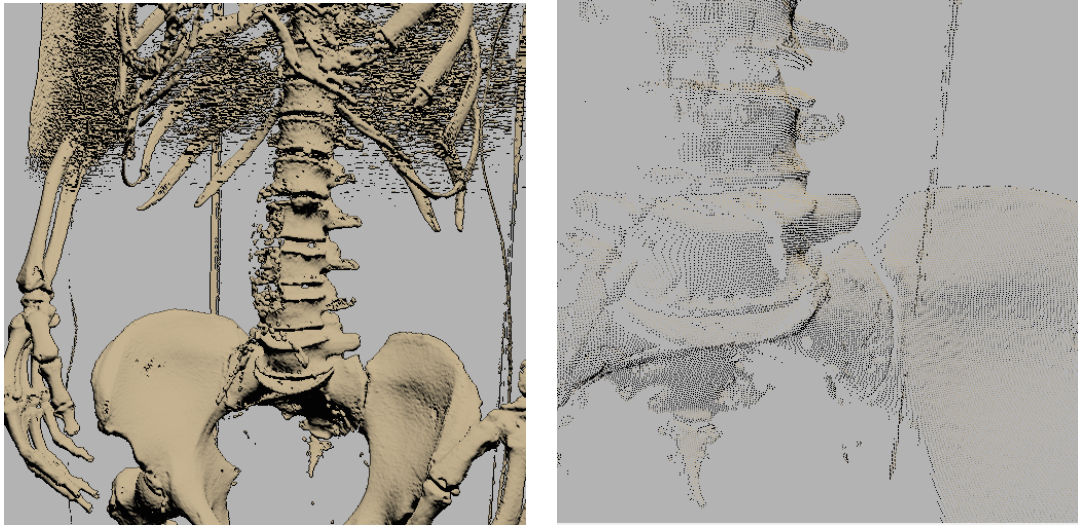


Fig. 11. Isosurface extraction of the full CT data (512 x 512 x 1734, 1mm spacing) of the NIH NLM Visible Female. **Left:** A section of the skeleton extracted by the PISA algorithm [33]. **Right:** A closeup view of the extracted points. Point shading is determined by an image-based normal computation technique that ensures high-quality results.

**Isosurface applications** As described above, isosurface extraction is a ubiquitous tool for exploring scalar volume datasets. The isosurface module in SCIRun software system (see the description in the Visualization Software section 7 below) supports the standard Marching Cubes algorithm as well as the high-performance NOISE algorithm. These tools are used for a variety of SCIRun applications, including isochrone visualization, isopotential surface visualization, and cutting plane synthesis, among others.

For example, SCIRun employs the isosurface extraction algorithm to produce and visualize isochrone surfaces, as demonstrated in Figure 12. In this application, the user can interactively step through different moments in time during cardiac activation to visualize how the activation wavefront passes through the heart tissue. By animating the isochrone value (time step), the electrophysiologist can investigate the specific processes and mechanisms involved in cardiac arrhythmia.

SCIRun also employs isosurface visualization to render and investigate how electrical activity on the cortical surface creates isopotential contours on the surface of the scalp. In Figure 13, we again illustrates how SCIRun can be used to visualize this data.

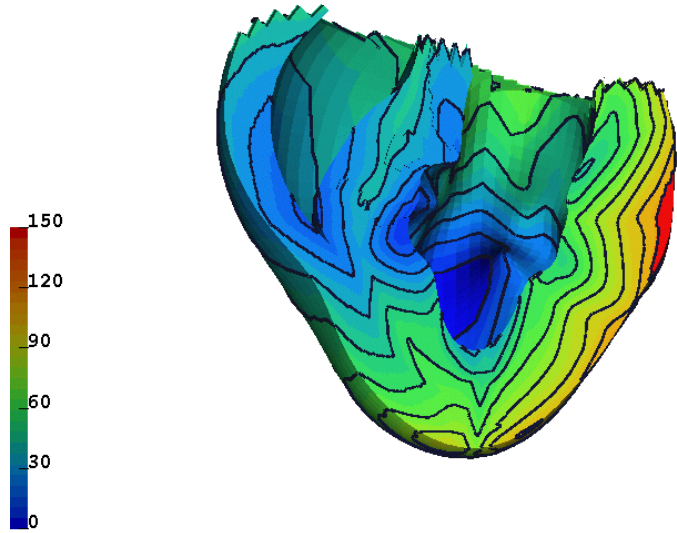


Fig. 12. BioPSE visualization of the isochrones for a cardiac activation simulation. The front of the heart has been clipped away to reveal the transmural activation times.

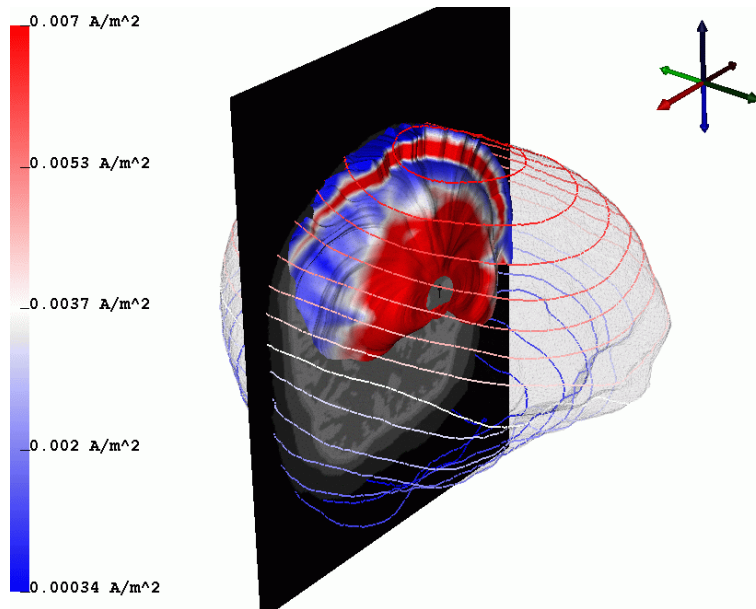


Fig. 13. Visualization of the potential distribution through the cranium due to a dipolar source simulation. Potentials are color-mapped onto a stream-surface within the head volume, and evenly spaced isopotential contours are plotted on the scalp surface. Data courtesy of Scott Makeig, UCSD and Greg Worrell, Mayo Clinic.

### 2.3 Time-dependent scalar field visualization

Temporal information can be incorporated and readily understood within volume rendering through the use of sequences of volume images generated across

a range of time steps. The use of such sequences allows one to effectively investigate a data set’s temporal dynamics, such as wave propagation effects through a three-dimensional scalar field. We have developed an algorithm that significantly reduces the time required to create flow animations of scalar fields while also reducing the storage requirements. This algorithm, called differential volume rendering[34], utilizes temporal and spatial coherence between consecutive time steps of simulation data to both accelerate the volume animation and to compress the volume data. The method may be used with all volume rendering techniques and can be adapted into a variety of ray casting paradigms that can be used to further accelerate the visualization process[35–37]. Additionally direct volume-rendering techniques have been proposed as a methodology to visualize scalar features in a dynamic time-dependent field[38–42].

### 3 Vector Field Visualization

Vector fields are a fundamental biophysical quantity that describe the underlying continuous flow structures of physiological processes. Examples of important biophysical vector fields include bioelectric fields, current densities, biomagnetic fields, as well the velocities and pressures of biofluids, and the forces associated with biomechanics. Vector-valued quantities also appear in biomedical data in the form of derivatives of scalar fields.

Common clinical examples of scalar fields associated with vector fields include electrocardiography (ECG) in cardiology, and electroencephalography (EEG) or magnetoencephalography (MEG) in neurology. Such measured clinical data is often sparse and noisy. In order to accurately approximate the associated vector fields of interest, a preprocessing stage is often needed that involves applying appropriate filtering and interpolation schemes. The derivatives of the resulting smooth quantities can then be computed to yield the vector fields. High-resolution vector fields are also directly obtained through computer simulations, including forward and inverse problems that rely on numerical approximation methods ranging from Finite Elements, Finite Differences, Finite Volumes and Boundary Elements. In these cases the vector field data naturally lends itself to scientific visualization techniques that respect the numerical models used in the computation.

#### 3.1 *Vector field methods in scientific visualization*

Visualizing vector field data is challenging because no existing natural representation can visually convey large amounts of three-dimensional directional

information. Visualization methods for three-dimensional vector fields must balance the conflicting goals of displaying large amounts of directional information while maintaining an informative and uncluttered display.

The methods used to visualize vector field data sets take their inspiration in real world experiments where a wealth of physical flow visualization techniques have been designed to gain insight into complex natural flow phenomena. To this end external materials such as dye, hydrogen bubbles, or heat energy can be injected into the flow. As these external materials are carried through the flow, an observer can track them visually and thus infer the underlying flow structure.

Analogues to these experimental techniques have been adopted by scientific visualization researchers, particularly in the computational fluid dynamics (CFD) field. CFD practitioners have used numerical methods and three-dimensional computer graphics techniques to produce graphical icons such as arrows, motion particles, and other representations that highlight different aspects of the flow.

Among existing flow visualization methods, the techniques relevant to the visual analysis of biomedical vector fields can be categorized as follows.

- (1) The simplest techniques correspond to an intuitive, straightforward mapping of the discrete vector information to so-called glyphs. Glyphs are graphical primitives that range from mere arrows to fairly complex graphical icons that display directional information, magnitude, as well as, additional derived quantities such as the curl and divergence altogether.
- (2) The second category corresponds to the set of techniques that are based on the integration of streamlines. Streamlines are fast to compute and offer an intuitive illustration of the local flow behavior.
- (3) Stream surfaces constitute a significant improvement over individual streamlines for the exploration of three-dimensional flows since they provide a better understanding of depth and spatial relationships. Conceptually they correspond to the surface spanned by an arbitrary starting curve advected along the flow.
- (4) Textures and other dense representations offer a complete picture of the flow, thus avoiding the shortcomings of discrete samples. Their major application is the visualization of flows defined over a plane or a curved surface.
- (5) The last type of flow visualization techniques are based on the notion of flow topology. Topology offers an abstract representation of the flow and its global structure. Sinks and sources are the basic ingredients of a segmentation of the volume into regions connecting the same spots along the flow.

Next we describe how each of these different approaches can be applied to the visualization of biomedical vector fields. Because of their lack of scalability and the strong occlusion issues that characterize them in practical applications we do not consider glyph-based techniques in further detail.

### 3.2 Streamline-based techniques

Streamlines offer a natural way to interrogate a vector data set. Given a starting position selected by the user, numerical integration over the continuous representation of the vector field yields a curve that can be readily visualized. The numerical schemes commonly used for the integration range from the first-order Euler scheme with fixed step size to Runge-Kutta methods with higher-order precision and adaptive step size [43]. The choice of the appropriate method requires to take into account the complexity of the structures at play and the smoothness of the flow.

Since streamlines are unable to fill the space without visual clutter the task of selecting an appropriate set of starting points (commonly called seed points) is critical to obtaining an effective visualization. A variety of solutions have been proposed over the years to address this problem. A simple interactive solution consists in letting the user place a rack in the data volume over which seed points are evenly distributed. The orientation and spatial extent of the rack, as well as the number of seed points can be adjusted to allow for the selective exploration of a particular region of interest, as shown in Figure 14.

Another class of methods aim at automatically placing seed points throughout the domain in order to achieve an even distribution of the corresponding streamlines [44–48]. Following this approach, Sachse et al. devised a new streamline seeding technique, specifically designed for the visualization of the electrical current, that distributes streamlines in the volume based on the local value of the current density [49,50]. As a result, streamline and current densities are proportional, which produce images that engineers can easily interpret. Examples are shown in Figure 15.

An additional limitation of flow visualizations based upon streamline techniques concerns the difficult interpretation of the depth and relative position of curves in a three-dimensional space. A solution consists in creating artificial lighting effects that emphasize curvature and assist the user in her perception of depth [51–53]. An alternative method that can be implemented on the graphics hardware, assigns a non-zero volume to individual streamlines. These streamlines are then depicted as tubes and filled with 3D textures to create expressive images in which various visual cues are used to enhance perception [54]. Refer to Figure 16.

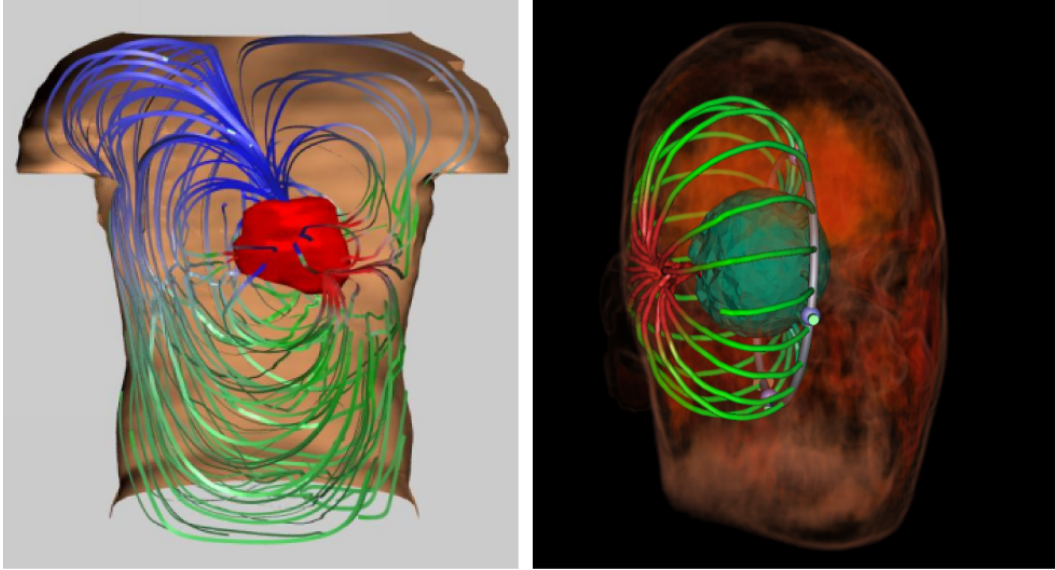


Fig. 14. Applications of streamlines to Finite Element biomedical data sets. **Left:** The bioelectric field in the torso visualized through streamlines seeded randomly around the epicardium. **Right:** Use of a circular rack to seed streamlines regularly around a dipolar source in the brain.

### 3.3 Stream surfaces

The intuitive representations offered by stream surfaces make them a very valuable tool in the exploration of three-dimensional flows. The standard method for stream surface integration is Hultquist's advancing front algorithm [55]. The basic idea is to propagate a polygonal front along the flow, while accounting for possible divergence and convergence by adapting the front resolution. Yet, this method yields triangulated surfaces of poor quality when the flow exhibits complex structures. We recently proposed a modified stream surface algorithm that improves on Hultquist's original scheme by allowing for an accurate control of the front curvature [56]. This method creates smooth, high-quality surfaces, even for very intricate flow patterns. We applied stream surfaces to the visualization of the cardiothoracic current obtained through a Finite Elements simulation [57]. Specifically, stream surfaces were shown to permit insight into the interconnection of different regions of the epicardium through the bioelectric current inside the thorax. An illustration is shown in Figure 17.

A similar approach was used to visualize the return current in a high-resolution simulation of a realistic head model. In this case stream surfaces proved instrumental in assessing the impact of various models of the white matter anisotropy on the current pattern and its interconnection with anatomical structures, see Figure 18 and section 5.1.

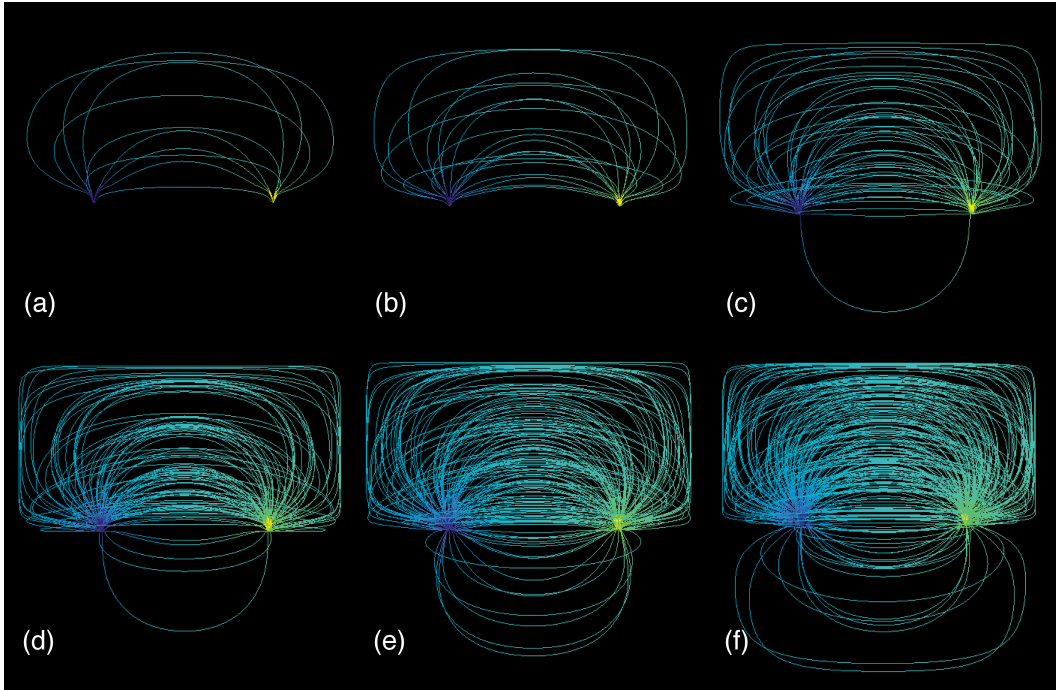


Fig. 15. Streamline visualization of electrical current flow in a cube. A conductivity of 0.02 and 0.2 S/m were assigned to the lower and upper half, respectively, of the cube. (a) 10, (b) 20, (c) 50, (d) 100, (e) 150, and (f) 200 streamlines were drawn. Two Dirichlet boundary conditions were assigned representing an electrical source and sink. A raster cube consisting of 32 x 32 x 32 cubic voxels constituted the spatial domain. Images courtesy of Frank Sachse [49]

Despite their esthetic appeal and the effective visualizations they yield, stream surfaces share with streamlines the limitation induced by their reliance on a careful seeding. Here, the seeding task consists in selecting a starting curve such that the resulting surface will exhibit the characteristic patterns of important flow structures. As with streamlines, this task can be tedious. In the case of the bioelectric current, flow structures can be defined in terms of interconnections between zones of inflow and outflow on a surface enclosing dipolar sources. This is the solution that we applied in Figures 17 and 18. To visualize the cardiothoracic current isocontours of either the electric potential or electric flux are used as seed curves on the epicardium, see Figure 17. In the case of the return current in the brain, however, no such obvious surface exists that encloses the source. A possible solution consists in introducing an artificial spherical surface surrounding the known source position. Refer to Figure 18, top left. Observe that culling is helpful to address the occlusion caused by the intricate shape of the stream surface.

Another solution to the seeding problem that we investigated consists in exploring the dependency of stream surfaces on a parameterization of their seeding curves. As the seeding curve changes according to some predefined mechanism the corresponding evolution of the stream surface can then be visualized

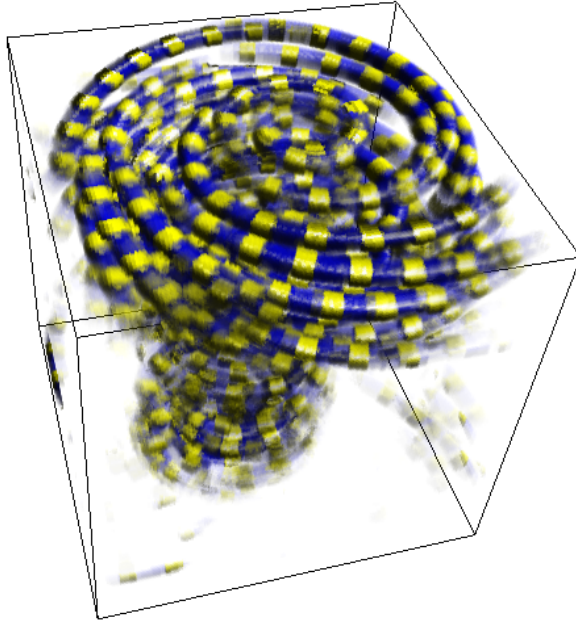


Fig. 16. An extension of streamline-based Flow Visualization. The image shows a combination of streamlines and 3D textures in the visualization of a tornado data set. Textures permit to embed additional information and ease the interpretation of the spatial context. From [54]

as an animation. For example this technique can be used to allow for a better understanding of the three-dimensional structure of the return current in the brain. Specifically, a circle of increasing radius centered around the dipolar source and lying in the transverse plane orthogonal to the dipole axis is regarded as a parameterized seeding curve. An analysis of the differences between isotropic and anisotropic conductivity of the white matter can then be made in a side by side comparison of the corresponding animations. Results are shown in Fig. 19.

### 3.4 Texture representations

Texture-based flow visualization methods provide a unique means to address the limitations of depictions based on a limited set of streamlines. They yield an effective, dense representation which conveys essential patterns of the vector field and does not require the tedious seeding of individual streamlines to capture all the structure of interest [58]. Arguably the most prominent of those methods is Line Integral Convolution (*LIC*) proposed by Cabral and Leedom [59]. The basic idea is to apply a one-dimensional low-pass filter to a white noise texture covering the two-dimensional flow domain. The filter kernel at each pixel is aligned with streamlines of the underlying flow. Consequently the resulting image exhibits a high correlation of the color values

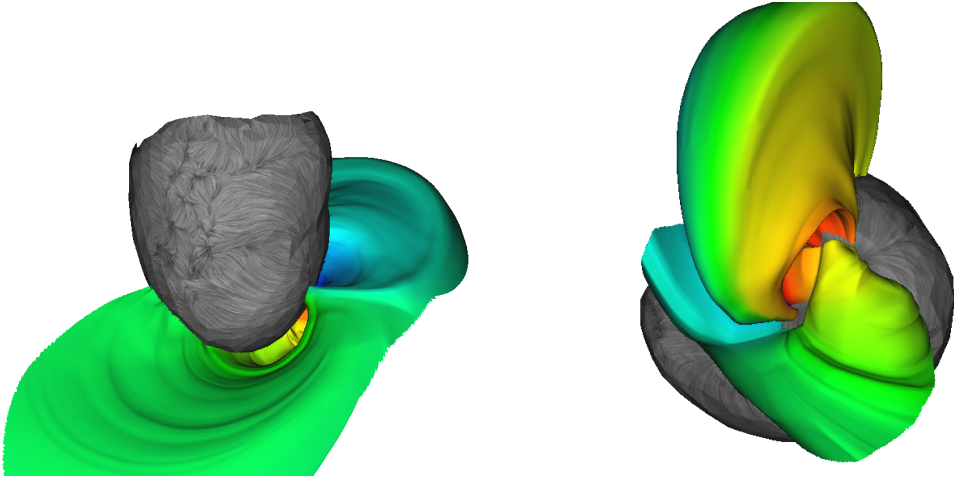


Fig. 17. Visualization of the bioelectric field in the direct vicinity of epicardium with high-quality stream surfaces. The image shows the technique applied to the cardio-thoracic current in a Finite Element forward computation. The surfaces capture the geometry of the current induced by the dipole equivalent cardiac source. They also provide an effective representation of the interconnections that exist between different regions on the epicardium. The seeding curves correspond to isocontours of the electric potential selected close to local extrema. A rainbow color map is used along each seeding curve to visualize flow stretch.

along the flow and little or no correlation across the flow. Hence this method produces a dense set of streamline-type patterns that fill the domain and reveal all the flow structures that are large enough to be captured by the fixed resolution of the texture. This seminal work has inspired a number of other methods. In particular, improvements were proposed to permit the texture-based visualization of time-dependent flows [60–62], flows defined over arbitrary surfaces [63–65], and dye advection [66]. Some attempts were made to extend this visual metaphor to three-dimensional flows [67,68].

An alternative to LIC-like visualization methods uses reaction-diffusion simulations to generate textures with shapes, sizes, and orientations driven by the underlying vector field[69]. Note that this approach to flow visualization is in fact an extension of a visualization method previously developed for diffusion tensors [14]. The human visual system naturally follows spatio-temporal patterns and can easily perceive very subtle changes affecting them. This allows the orientation and magnitude of the local vector field to be conveyed with an appropriately tuned pattern of elliptical spots. This method of visualization is based on mapping two of the vector field components, orientation and magnitude, to the diffusion kinetics in the reaction-diffusion system. Our method also supports mapping orientation *uncertainty* to the diffusion kinetics. This is further discussed in section 5.2. The principal advantage of the reaction-diffusion model over existing flow field visualization techniques is that the pattern size and density that naturally arises from the reaction-diffusion model accurately represents the underlying vector field, based on a

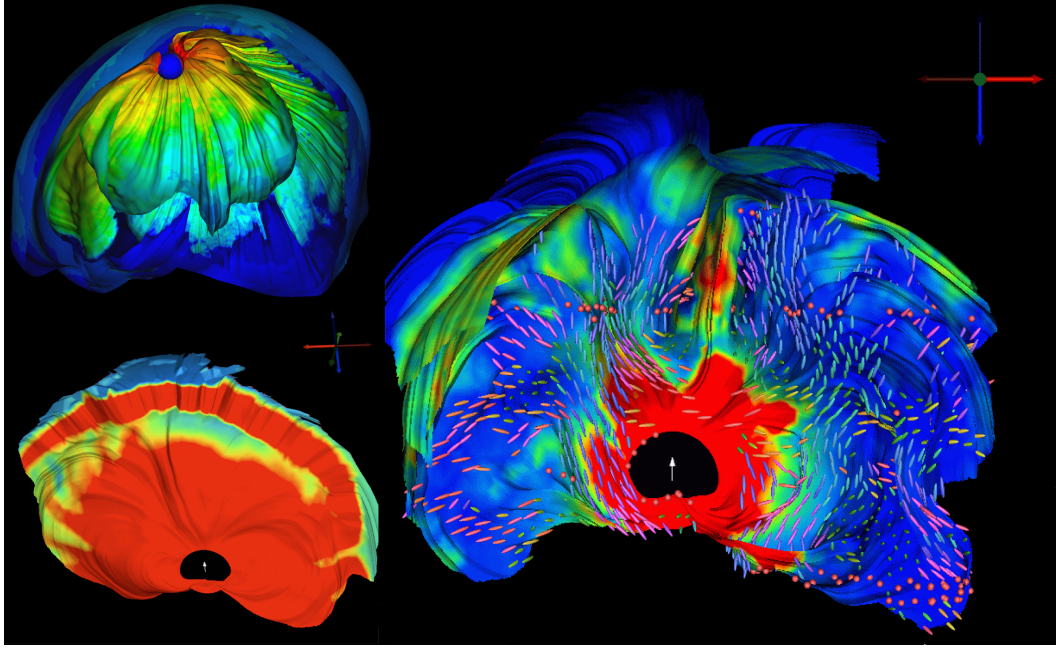


Fig. 18. Stream surface visualization of bioelectric field induced by a dipolar source in left thalamus. **Left top.** Stream surfaces seeded along isocontour of electric flux on sphere enclosing the source. Culling is used to address occlusion. White matter has anisotropic conductivity. **Left bottom.** Stream surface started along circle contained in coronal slice and centered around source location. White matter is assumed isotropic. Color coding corresponds to magnitude of electric field. **Right.** Similar image obtained for anisotropic white matter. Glyphs visualize major eigenvector of conductivity tensor. Color coding shows magnitude of return current.

flexible mapping from multiple field characteristics to parameters of the diffusion kinetics. Figures 20 and 21 show the anisotropic diffusion applied to the Turing[70] and Gray-Scott[71,72] reaction-diffusion models for a vector field at 45 degrees with a random variation in the magnitude.

From the point of view of their application to biomedical vector data texture representations can be seen as the natural vector counterpart of color plots for scalar potentials. Indeed, this type of technique is best suited for the visualization of flow data defined over a plane or a curved surface. Moreover, texture-based visualizations can be combined with the color coding of a scalar quantity associated with the vector field to enrich the pictures.

An important property of bioelectric fields is their homogeneous Neumann boundary condition which imposes that the current cannot leave the conductive volume and therefore must be tangent to its boundary. In particular, the current is tangential to the torso and the scalp. In contrast the epicardium surface is crossed by the current originating at sources locations contained in the cardiac tissue. As a consequence, the visualization of the restriction of the current to the heart surface by means of textures requires to first project it

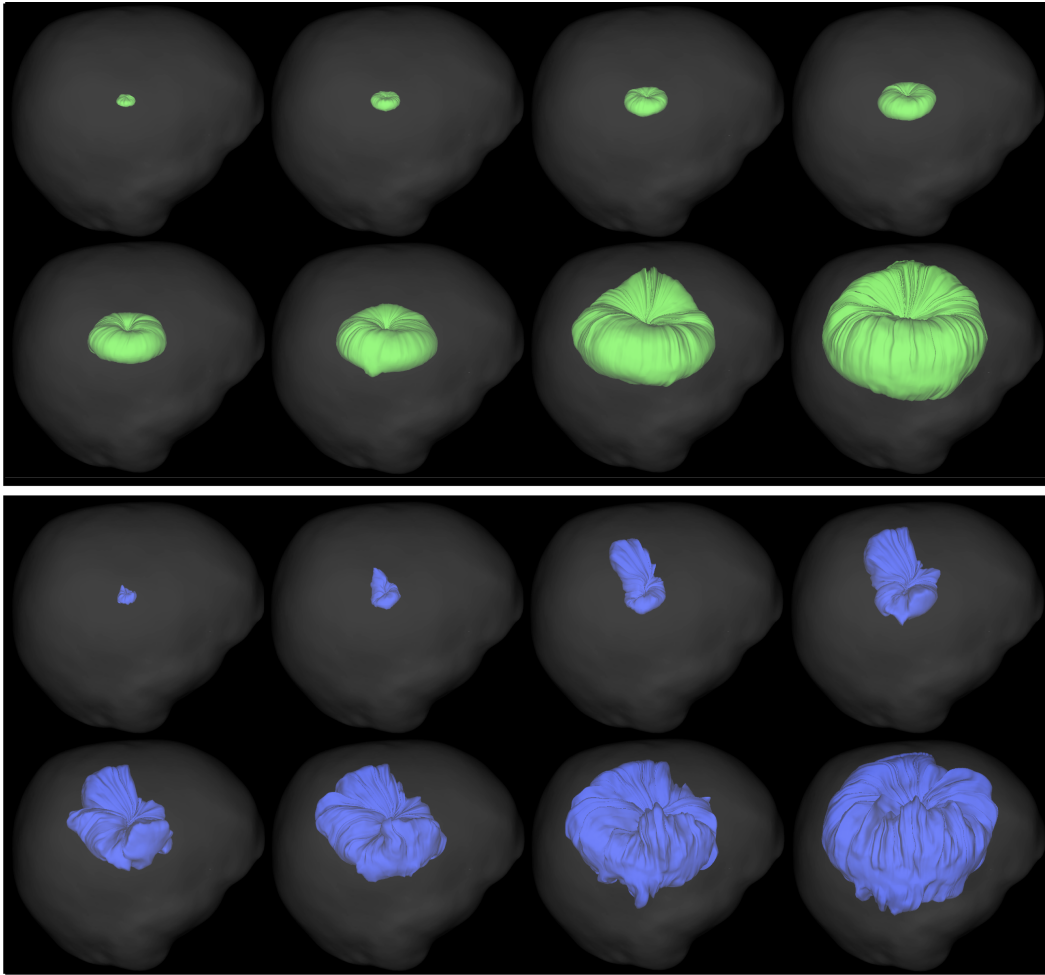


Fig. 19. Evolution of a stream surface integrated along the return current with respect to the increasing radius of its seeding circle. **Top row.** Frames from an animation corresponding to isotropic white matter. **Bottom row.** Frames of the animation obtained for anisotropic white matter.

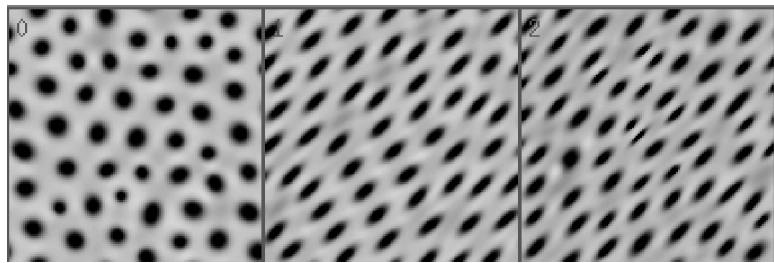


Fig. 20. Turing model visualization of a vector field with a) random magnitude b) constant orientation c) magnitude and orientation.

onto the corresponding geometry. Examples are proposed in Figure 22, left, and Figure 25.

Similar to color plots, an obvious way to address the occlusion problems encountered when applying texture visualizations to volume data is to restrict

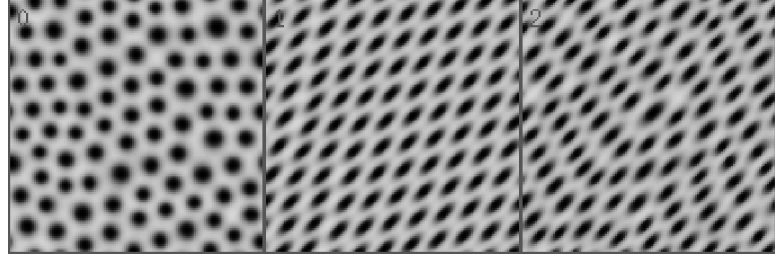


Fig. 21. Gray-Scott model visualization of a vector field with a) random magnitude b) constant orientation c) magnitude and orientation.

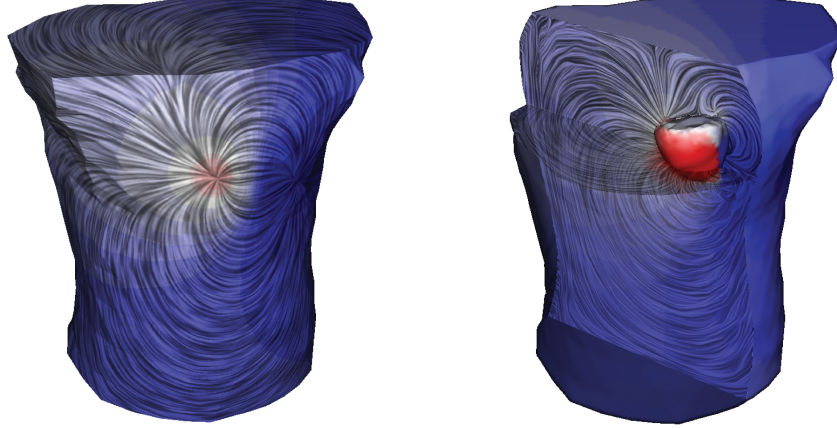


Fig. 22. **Left.** LIC representation of the current on the boundary of a Finite Element grid used in forward computation. The color coded electric potential (negative values in blue, positive values in red) are superimposed on the texture. **Right.** Two LIC textures computed over cutting planes combined by transparency. The geometry of the heart remains opaque for context.

the representation to a cutting plane. To be meaningful the choice of this plane must be made based on the symmetry of the geometry and on the known position of a bioelectric source, see Figure 22, left and Figure 23. However, a single plane is typically unable to convey an informative picture of the three-dimensional current. This problem is emphasized when the conductivity of the tissue is anisotropic which breaks the symmetry of the dipolar current flow pattern and increases its geometric complexity. A simple solution consists in displaying two or more such planes in combination. Additionally transparency allows the user to see the spatial relationship between the patterns exhibited by each texture. An example is shown in Figure 22, right.

### 3.5 Topology

The topological approach provides a powerful framework for flow visualization in a broad range of applications [73]. For planar vector fields, as well as vector fields defined over curved surfaces, it has established itself as a method of ref-

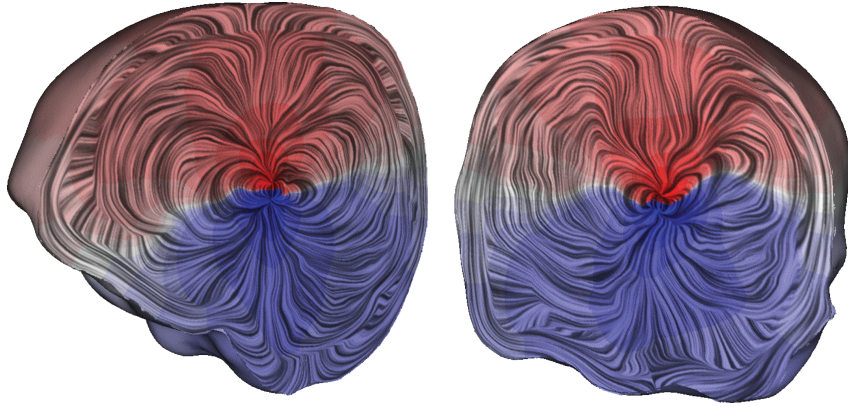


Fig. 23. LIC applied to coronal and sagittal clipping planes reveals details of the dipolar source and its interaction with the surrounding anisotropic tissue. Rather than a typical smooth, symmetric dipolar pattern, the electric current is clearly diverted by the presence of white matter tracts that lie close to the source. The field also changes direction very rapidly as it approaches the skull just beneath the surface of the head.

erence to characterize and visualize flow structures. The excessive complexity of the topology of intricate flows can be addressed by simplifying the resulting graphs while preserving essential properties in order to facilitate the analysis of large-scale flow patterns [74,75]. Refer to Figure 24.

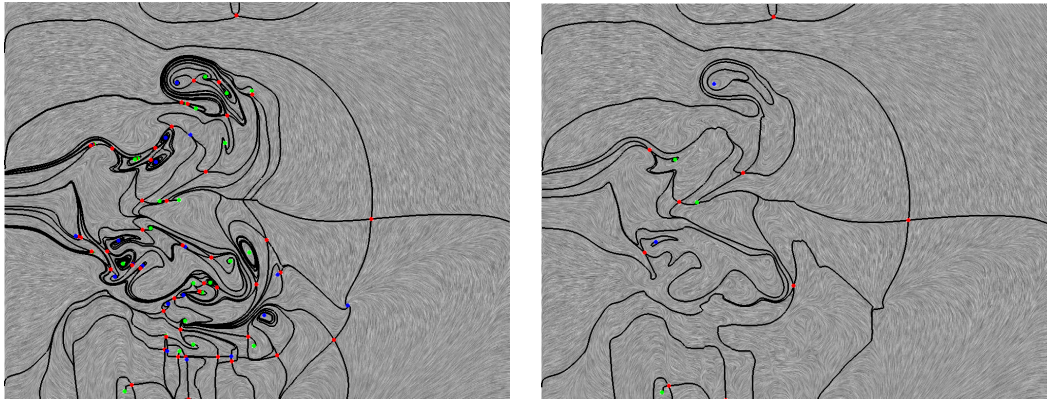


Fig. 24. Topology simplification. The left image shows the original topology obtained for a CFD simulation of a streaming jet with inflow into a steady medium. Numerous small-scale structures lead to a cluttered depiction. The right image shows the same data set after topology simplification.

Topology-based methods prove interesting in the visualization of the bioelectric current on the epicardium. In this case, the automatically extracted topological features are believed to be related to what is known in cardiac electrophysiology as epicardial breakthroughs. This phenomenon occurs when an activation wave in the cardiac tissue breaks through the surface, generating a local potential minimum in the epicardial surface. Refer to Figure 25.

The usability of three-dimensional topology for the characterization of salient

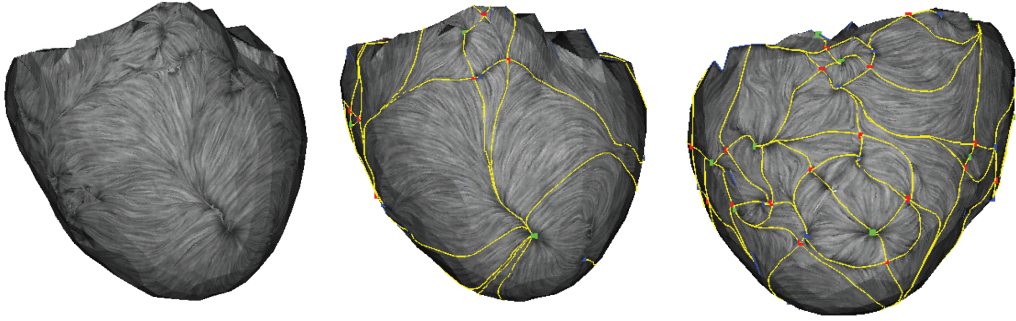


Fig. 25. Topology of bioelectric field on epicardium. The images show a LIC representation of the potential gradient on the surface enhanced by the depiction of the associated topological graph. Green points correspond to potential minima, blue points mark potentials maxima. Left and middle images show an anterior view of the epicardium. Right image shows a view of the torso from the left.

patterns of the bioelectric current remains limited. The explanation comes from the structure of a bioelectric field. Indeed, bioelectric sources typically behave as dipoles, which do not exhibit an intrinsic separation surface and therefore do not allow for a natural topological segmentation of their surrounding medium. However the application of the topological framework to the visualization of bioelectric activity is at a very early stage and future research will be necessary to determine the full potential of this approach.

Beyond its application to bioelectric data, the topological approach shows great promise to be instrumental in the structural investigation of flows in other biophysical fields as well. For instance, topology is known to permit the characterization of flow recirculation patterns in fluid dynamics [76] and can therefore provide powerful tools to analyze blood recirculation in hemodynamics. Topology could also be used to study and visualize the structures of forces in biomechanics.

#### 4 Tensor Field Visualization

Tensors provide the language necessary to describe the intrinsic material properties of biological systems. Electrical conductivity and molecular diffusivity are examples of material properties that describe the ability of particles (such as electrons and water molecules) to pass through a given material. Strain and stress tensors on the other hand, characterize the mechanical properties of soft tissues. Material properties are often *inhomogeneous*, that is they vary as a function of the position within the material. Thus, proper modeling of their characteristics requires a field of tensor values sampled in three dimensions. Hence gaining insight in the structure of three-dimensional tensor fields is a

significant and ongoing challenge in biomedical visualization.

The need for tensor visualization arises in the modeling of the material conductivity of tissue, such as in the brain or heart. Conductivity is a tensor quantity because the fiber structure of the tissue results in anisotropic conduction [77,78]; setting accurate values of fiber structure is a crucial component of a model of the cardiac propagation [79,80], or the localization of an epileptic seizure from an inverse EEG computation, tasks that require tensor field visualization capabilities.

Another application that has drawn increasing interest is diffusion tensor imaging. Diffusion tensor MRI (DT-MRI or DTI) is an imaging modality that permits, through its influence on the local diffusion of water molecules[81], the non-invasive measurement of tissue physical microstructure. In regions where the tissue has a linear organization, such as in myelinated axon bundles comprising the white matter in the brain or in muscle tissue, diffusion is preferentially directed along the fiber direction, and this phenomenon can be measured with DT-MRI. Creating meaningful images or models from diffusion tensor data is challenging because each sample point has six independent degrees of freedom.

The deformation of the heart muscle (myocardium), namely its successive contraction and expansion are described by a different tensor, the strain tensor. For clinical purposes the analysis of the strain tensor field in the left ventricle is of great significance in the efficient screening of cardiac patients since abnormal properties of the myocardial strain can be identified before the first symptoms of a heart attack [82]. An imaging technique used to acquire the corresponding tensor data is called *Tagged MRI*. It consists in using radiofrequency pulses in a MR scanner to create dark lines in the MR image. Because these lines deform with the tissue, the motion of material points can be tracked over time to compute the strain tensor [83]. Measures obtained through MRI can be coupled with Finite Element models of the mechanics of the tissue [84] or deformable image registration [85]. The visualization of the resulting tensor data is then instrumental in producing diagnostic information for cardiac conditions.

The remainder of this section provides an overview of the different visualization techniques that have been devised to help clinicians and researchers explore and analyze the rich structural information contained in large biomedical tensor data sets.

#### 4.1 Anisotropy and tensor invariants

The examples of tensor fields mentioned previously share the property that they correspond to real symmetric maps between vector fields. Real symmetric tensors have real eigenvalues  $\lambda_i$  and the associated eigenvectors  $\vec{e}_i$  are mutually orthogonal:

$$T\vec{e}_i = \lambda_i \vec{e}_i, \quad \lambda_i \in \mathbb{R}, \quad \forall i \neq j \quad \vec{e}_i \cdot \vec{e}_j = 0.$$

A standard notation consists in classifying the 3 eigenvectors in major, medium, and minor eigenvectors with respect to the corresponding eigenvalue:  $\lambda_1 \geq \lambda_2 \geq \lambda_3$ .

A tensor is called *isotropic* if it maps every vector direction uniformly. In the case of a diffusion tensor, for example, this corresponds to an equal passage of molecules through the material in every direction. An isotropic strain tensor indicates that the material deforms uniformly in all directions. This property implies that all eigenvalues are equal and individual eigenvectors in the previous definition cannot be characterized (the eigenspace is three-dimensional). When there exists a preferred direction, the tensor is called *anisotropic*. Two different anisotropic behaviors exist for three-dimensional tensors. *Linear anisotropy* corresponds to one large and two small eigenvalues:  $\lambda_1 \gg \lambda_2 \approx \lambda_3$ . In this case a single preferred direction exists. *Planar anisotropy* corresponds to two large and equal eigenvalues and a small third eigenvalue:  $\lambda_1 = \lambda_2 \gg \lambda_3$ . In this case, the restriction of the tensor to its two-dimensional eigenspace is isotropic. To characterize the anisotropy of a tensor several measures have been devised that find direct applications in biomedical tensor visualization. Basser and Pierpaoli introduced the notion of *fractional anisotropy* [86] defined as:

$$\text{FA} = \sqrt{\frac{3}{2} \frac{\|T - \mu_1 I_3\|}{\|T\|}},$$

where  $\mu_1 = \frac{1}{3} \sum_i \lambda_i$  is the mean of the eigenvalues,  $I_3$  is the identity map, and  $\|\cdot\|$  designates the Frobenius norm. The term  $T - \mu_1 I_3$  is obtained by subtracting the isotropic part of tensor  $T$  and is called its *deviator*. FA measures the anisotropy of a given tensor but does not differentiate between linear and planar anisotropy. To address this limitation Westin proposed three metrics that quantify linear and planar anisotropy, as well as isotropic behavior [87].

$$c_l = \frac{\lambda_1 - \lambda_2}{\lambda_1 + \lambda_2 + \lambda_3}, \quad c_p = \frac{2(\lambda_2 - \lambda_3)}{\lambda_1 + \lambda_2 + \lambda_3}, \quad c_s = \frac{3\lambda_3}{\lambda_1 + \lambda_2 + \lambda_3}$$

Observe that eigenvalues as well as quantities derived from them are invariant under changes of the reference frame. As such they correspond to intrinsic properties of the tensor and are of primary interest for visualization purposes.

#### *4.2 Color coding of major eigenvector orientation*

A solution to visualize the directional information associated with the major eigenvector consists in using a spherical color map. The coordinates of the major eigenvector in the reference frame of the laboratory are mapped to red, green, and blue color values. Because of the indeterminacy of an eigenvector's direction, both  $e_1$  and  $-e_1$  are mapped to the same color. Additionally, the orientation of the major eigenvector is poorly defined when the eigenvalues approach planar anisotropy. Therefore the saturation of the color is set with respect to the value of the linear anisotropy metric  $c_l$ , which measures the significance of the major eigenvector as a means to assess the anisotropy of the tensor. Pajevic and Pierpaoli analyzed the perception issues associated with different color maps following this basic principle [88].

#### *4.3 Tensor glyphs*

At the small scale, glyphs are a staple of tensor visualization because they provide an intuitive display of individual tensor samples by mapping the eigenvalues and eigenvectors of each tensor to the shape and orientation of a geometric element such as a box or ellipsoid [3]. Observe that as opposed to diffusion or conductivity tensors whose eigenvalues are positive by definition, strain tensors can have both positive and negative eigenvalues, corresponding to stretch and compression respectively. Therefore Wünsche and Young [84] suggested to alternate between a red and a blue color coding mapped onto ellipsoid glyphs to disambiguate the sign of the eigenvalues. Data inspection with glyph-based methods represents the first phase of understanding structures in a tensor field. The use of traditional glyphs for diffusion tensor visualization has a number of drawbacks. While ellipsoidal glyphs are mathematically simplest because their symmetry can directly convey a tensor eigensystem, their round shape may not effectively indicate vital shape and orientation cues, a problem that may lead to ambiguous displays of disparate tensor values. Cuboid glyphs, with their sharp edges, avoid this problem, but, in the case of eigensystem symmetry (eigenvectors are not unique when two or more eigenvalues are nearly equal), they often depict an arbitrary directional information, which is easily influenced by noise.

Westin et al. proposed to address that limitation by mapping the metrics  $c_l$ ,  $c_p$ , and  $c_s$  introduced previously to a line, a disk, and a sphere primitive combined

in the same glyph [89]. Kindlmann recently presented an alternative strategy employing a glyph geometry that changes according to the tensor eigensystem, emphasizing directional information only where it is numerically well-defined and otherwise reverting to symmetrical configurations [90]. A technique of solid modeling called *superquadrics* allows him to represent cuboids, ellipsoids, cylinders, and all intermediate shapes. Figure 26 demonstrates the palette of super quadric glyphs, in which the extremes of spherical, linear, and planar anisotropy occur at the corners of the triangle.

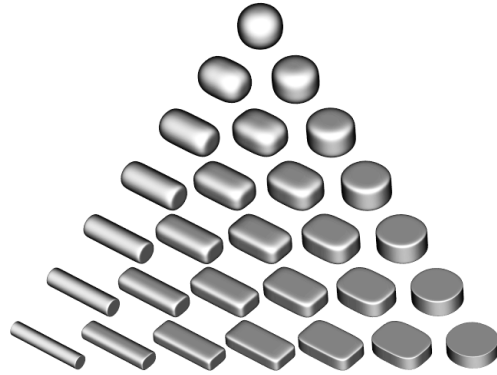


Fig. 26. Superquadric tensor glyphs smoothly blend between cylinders, boxes, and spheres. From [90]

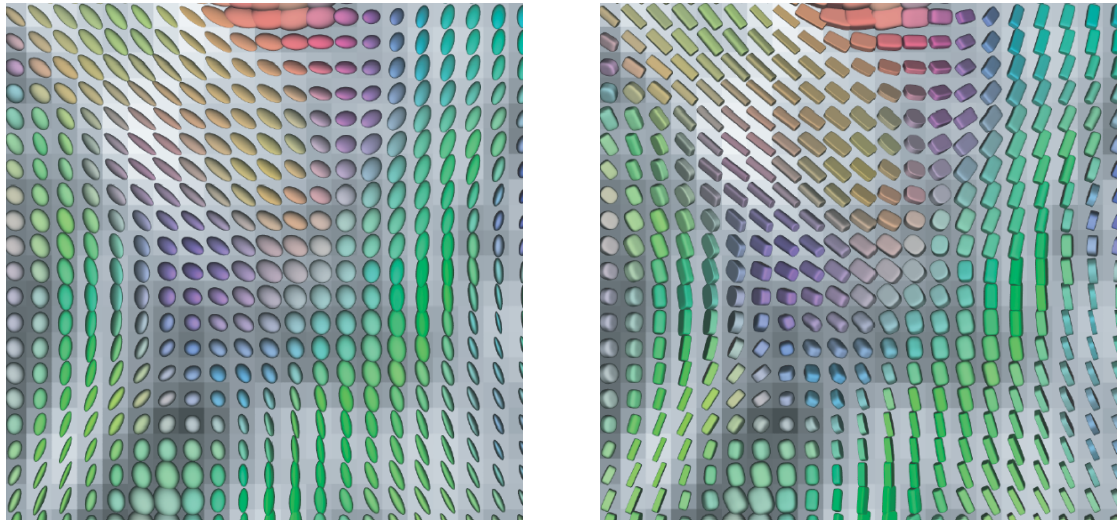


Fig. 27. Ellipsoidal (left) and superquadric (right) glyph visualizations of an axial slice of a DT-MRI scan.

Figure 27 demonstrates the differences between ellipsoidal and superquadric glyphs as used to visualize tensor field data from an axial slice of a diffusion-tensor MRI dataset. In the left side of Figure 27, many of the ellipsoidal glyphs appear similar, while the shape differences are more clearly conveyed with the superquadric glyphs in the right side of Figure 27. The superquadric glyphs additionally clarify directional patterns. Ideally, the composition of multiple glyphs from across the tensor field can hint at larger-scale features that may

be subsequently explored and extracted with other visualization and analysis techniques.

As with vector visualization, simple attempts at indicating all the tensor variables at all sample locations rapidly produces unintelligible visual clutter. In DT-MRI of nervous tissue, the degree of anisotropy has a biological significance relating to the white matter structure, so an effective way to avoid clutter is to display only those tensors that exhibit anisotropy of a certain degree or greater. This strategy was used in Figure 28.

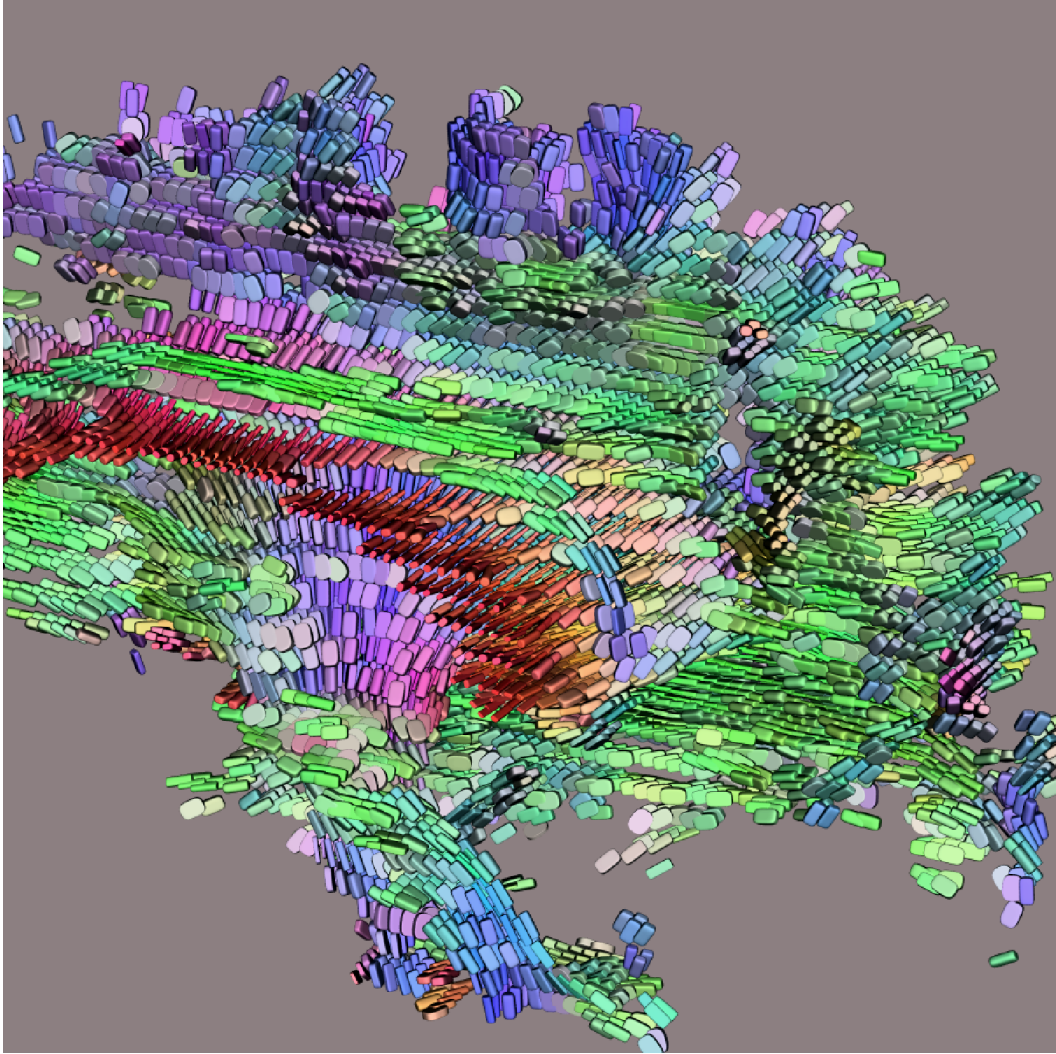


Fig. 28. Visualization of half a brain DT-MRI volume using superquadrics glyphs. Glyphs are depicted only in anisotropic voxels. Red indicates left/right fiber orientation, green indicates anterior/posterior, and blue indicates superior/inferior. Image courtesy of Gordon Kindlmann.

Alternatively, the visualization can be restricted to a single slice. For this type of representation Laidlaw et al. proposed a method to normalize the size of the ellipsoids and another method that leverages techniques from oil painting

to offer a complete view of the tissue anisotropy on a given slice [91].

While the symmetric tensor is a popular representation for the local diffusion, it is a simplification of the underlying biophysics. In reality, how water diffuses from a local region varies continuously over the space of directions. A tensor representation approximates that continuous distribution with an ellipsoidal shape parameterization. However, with the emerging field of high angular-resolution diffusion (HARD) imaging, more complicated shapes can be measured and represented. HARD images reveal complex patterns at fiber-crossing locations within the brain. This intravoxel heterogeneity is demonstrated in Figure 29)[92,93].

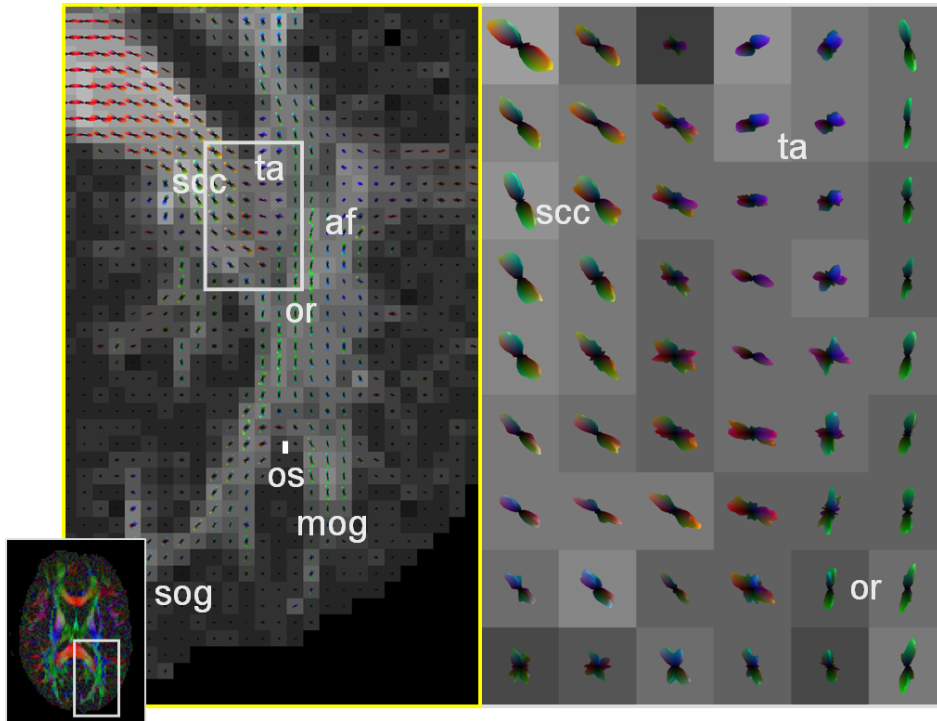


Fig. 29. Q-ball image showing intravoxel fiber crossing in the major forceps. Figure courtesy of D.S. Tuch.

In these images, the non-ellipsoidal shape of each glyph is exaggerated by subtracting the isotropic component from the local measurements.

#### 4.4 Fiber tractography

In diffusion tensor MRI, a popular technique of feature extraction is fiber tractography[94–96]. In DT-MRI of nervous tissue, fiber tractography seeks to create models of the pathways of axon bundles in white matter tracts. In muscle tissue, such as the myocardium of the heart, tractography can illustrate

the directional structure of the muscle fibers. Standard methods of tractography are essentially applications of hyperstreamlines[97,84], in which pathways are numerically integrated along the direction of the principal eigenvector of the tensor samples. The biological justification for this lies in how the direction of greatest diffusivity, the principal eigenvector of the tensor, should indicate the orientation of the fibrous microstructure of the underlying tissue. However, noise in the data, inadequate resolution, or complex structures may lead to problems in the visualization. In such cases, the direction of the principal eigenvector changes suddenly or is not numerically well defined.

To address this, several generalizations of standard fiber tractography have been proposed. *Tensorlines* [98] add an advection term to the diffusion equation in order to numerically stabilize the path integration. Zhang et al. created a visualization method that constructs tubular representations of fiber pathways in region of strong linear anisotropy and surfaces everywhere tangential to the two-dimensional eigenspace in regions of planar anisotropy [96]. Surfaces provide an intuitive depiction of the directional information associated with planar anisotropy while avoiding the numerical instability associated with the tracking of the ill-defined major eigenvector. The scheme computes both *streamtubes* and *streamsurfaces* everywhere in the domain. It then applies a decimation procedure that preserves the geometric structures only where they are most meaningful and prunes objects based on similarity measures. Zhukov and Barr presented a solution to the problem of tracking fiber orientation across noisy DT-MRI data [99,100]. Their approach uses a regularization method during the integration based on the technique of Moving Least Squares. It determines the local tracking direction as a combination of the orientation sampled in a neighborhood of the current position. The shape and extent of the neighborhood is determined by a gaussian weighting function that is scaled in each direction with respect to the anisotropy of the fiber direction determined in the previous iteration. The application of this method to white matter and cardiac tissue shows the robustness of this strategy and its ability to extract subtle pathways. Illustrations are proposed in Figure 30 and Figure 31.

Alternatively, Hlawitschka and Scheuermann proposed an algorithm for fiber tracking in HARD tensor data called *HOT-Lines* [101]. Due to the higher angular resolution crossings and bending of neural fibers within a single voxel can be detected which is not possible using second order tensor models. The method computes the fiber directions by means of a gradient descent algorithm and therefore extracts fiber pathways that fully leverage the high angular accuracy available in the input data.

A natural extension of fiber tractography consists in grouping individual pathways together to yield a segmentation of the white matter into fiber bundles. From a visualization standpoint, the result of this clustering task can also

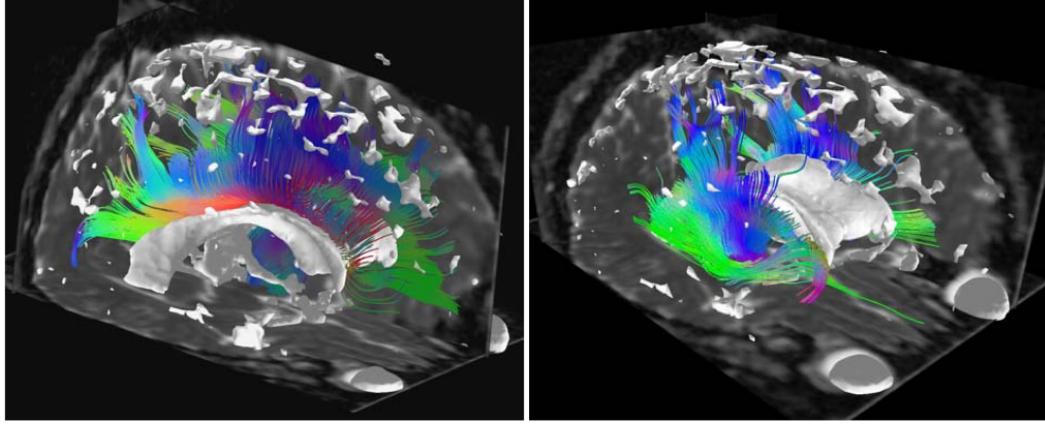


Fig. 30. Brain structures: neural pathways computed using the MLS algorithm in the corpus callosum (left) and corona radiata (right) shown together with isotropic brain structures - ventricle, eye sockets, and pockets of CSF on the top of the brain. Cutting planes show isotropic  $c_s$  values. Images courtesy of Leonid Zhukov [99]

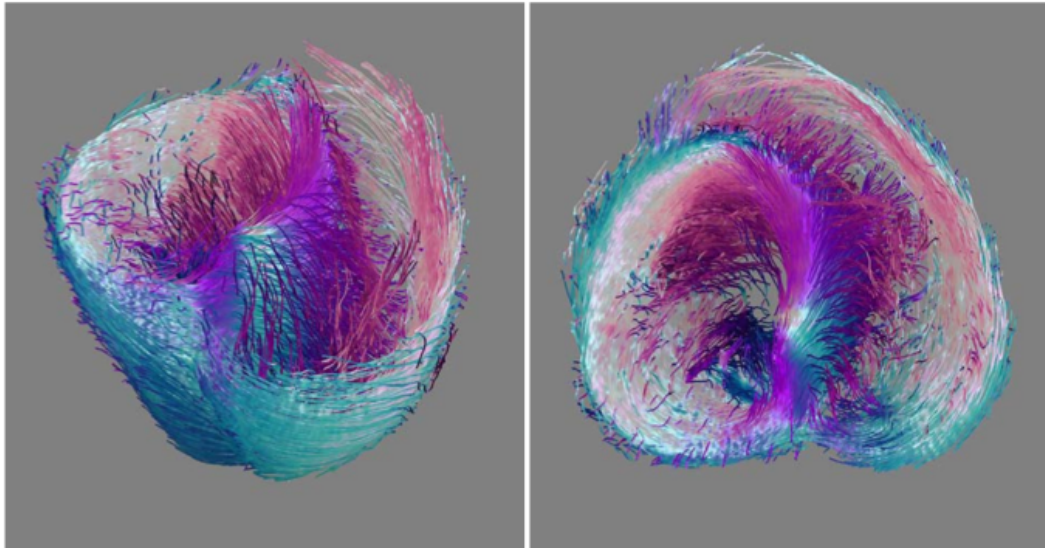
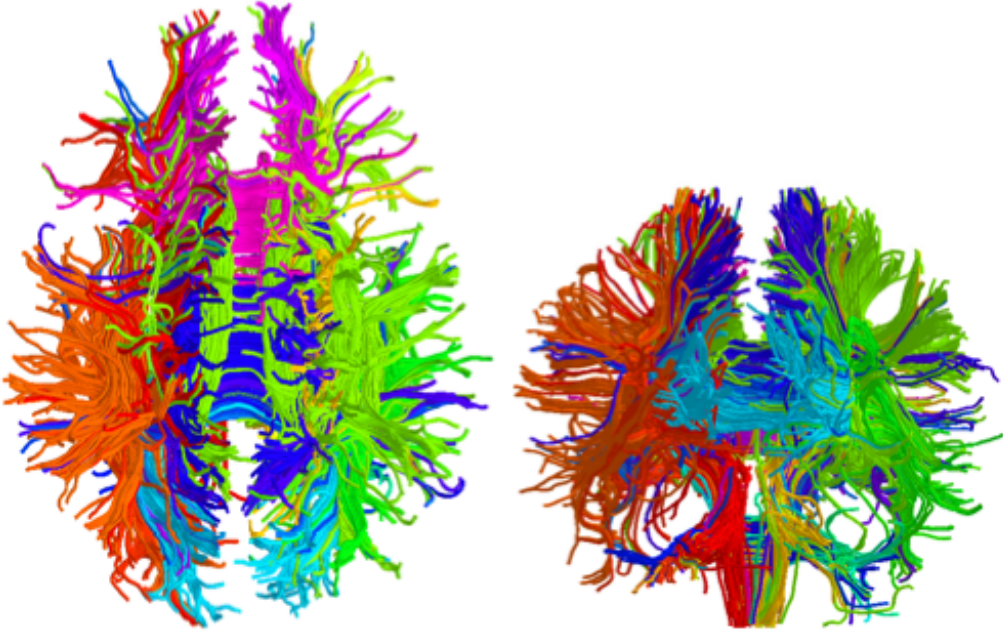


Fig. 31. Reconstruction of heart muscle fibers using the MLS algorithm. The color coding changes smoothly from clockwise to counterclockwise spiral oriented fibers. Horizontal parts (very small pitch angle) of the fibers are shown in white. This coloration is consistent with observations of some heart researchers, who have described a systematic smooth variation in pitch and direction of heart muscle fibers from endocardium to epicardium. Images courtesy of Leonid Zhukov [100]

be leveraged to provide a color coding of the fibers that enhance the interpretation of their spatial structure and their anatomical significance [102]. Some methods require the user to guide the clustering, typically by specifying one or several regions of interest (ROI) [95,103] in order to identify the fibers that intersect them. In the case of several ROIs, boolean logic can be applied to determine the set of fibers that connect known regions of the brain anatomy [104–106]. Clustering can also be achieved in a non-supervised way.

To that end, Brun et al. proposed to represent each fiber pathway in a high-dimensional space that embeds the mean vector of the fiber as well as its covariance matrix [107]. In that space the authors apply so-called *normalized cuts* that iteratively split the set of fibers in halves until some homogeneity criteria are met in each cluster. The result of their method is shown in Figure 32. Alternatively, Zhang and Laidlaw used an agglomerative hierarchical clustering method [108].



**Fig. 32. Left:** Axial view of a segmentation obtained from recursive bipartitioning of the white matter fiber traces. The color of fiber traces indicate cluster membership. **Middle:** coronal view. Images courtesy of Carl-Fredrik Westin [107]

#### 4.5 Volume rendering

Beyond its traditional application to the visualization of three-dimensional scalar fields, direct volume rendering has also been extended to tensor fields in several ways. Wenger et al. [109] generalized ideas previously used to visualize vector fields to achieve the volume rendering of diffusion tensor fields. The basic ingredients of their representation are threads that depict the directional information contained in the data combined with halos that enhance depth perception and whose color and opacity can be varied to encode a scalar measure of anisotropy. Following a different approach, Kindlmann et al. proposed to use the barycentric coordinates of anisotropy measure introduced in section 4.1 to control the opacity of the data volume [110,111], see Figure 33.

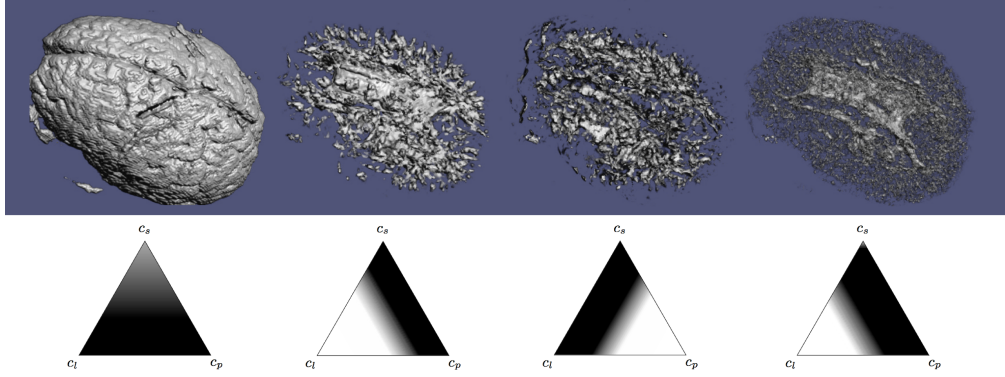


Fig. 33. Examples of barycentric opacity maps and resulting volumes. Brighter regions in the triangle correspond to higher opacity assignment. From [111]

The additional use of a standard color map indicating the orientation of the major eigenvector helps disambiguate distinct structures of the white matter. The same authors also designed a method called *Lit-Tensors* that provides visual clues about the type of anisotropy and the corresponding orientation. Their idea consists in introducing an additional control parameter in the standard Blinn-Phong shading model that allows for a smooth transition between shading models associated with line and surface objects respectively. In that way regions of linear anisotropy are shaded like illuminated streamlines [112] and regions of planar anisotropy are shaded like surfaces, while intermediate anisotropy types are shaded according to a combination of these two extrema. Moreover this method can be combined with a shading based on the gradient of an opacity function alone, which ensures a consistent shading across a feature of interest. Refer to Figure 34.

In his PhD thesis [113] Kindlmann also described a volume rendering method based on the analytical computation of the derivatives of a tensor invariant like FA. Leveraging smooth reconstruction kernels for the computation of the tensor invariant and its derivatives, the method is able to generate volume renderings of extremely high-quality that effectively captures anatomical structures.

#### 4.6 White matter segmentation using tensor invariants

We mentioned previously that fiber tractography can serve as a basis for segmentation of the white matter into bundles of neural pathways that exhibit strong spatial similarities. In collaboration with G. Kindlmann and C.-F. Westin from Harvard Medical School we have recently proposed a compelling alternative to that approach [114] which does not require the potentially error-prone integration of fiber tracts in noisy tensor data. Leveraging concepts from the field of computer vision we have devised a method that computes

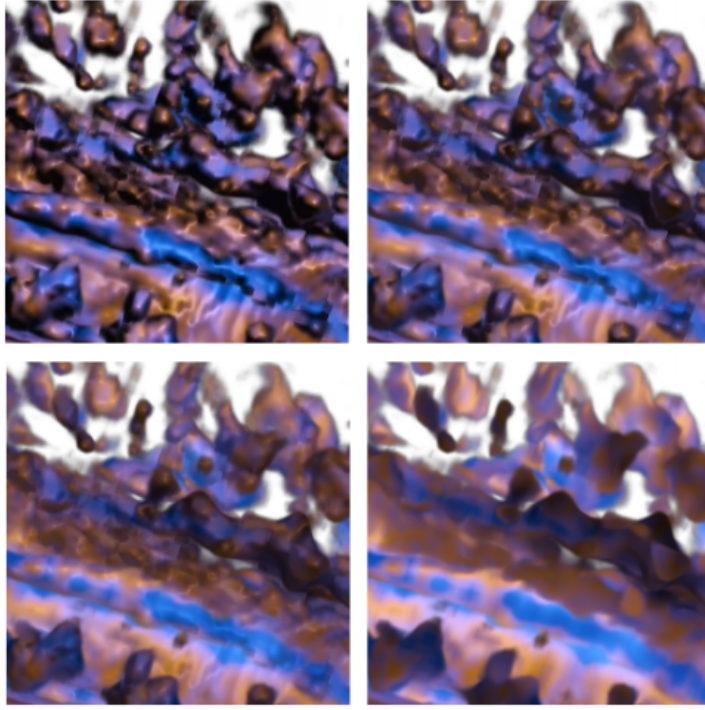


Fig. 34. Mixing between lit-tensor and opacity gradient shading for a portion of brain data. Images from [111]

a segmentation of the white matter tissue through crease surfaces of the tensor invariant FA. The premise of this technique is that surfaces where the anisotropy (as measured by FA) is locally maximal (ridges) correspond to the two-dimensional core of a fiber bundle, while surfaces where FA is locally minimal (valleys) coincide with the boundary between adjacent but distinctly oriented fiber tracts. The algorithm makes use of cubic separable reconstruction kernels so as to permit the analytical computation of the smooth second-order derivatives needed to identify crease surfaces. The results demonstrate the anatomic relevance of the structures extracted in that way. An illustration is proposed in Figure 35.

## 5 Uncertainty

### 5.1 Multi-field visualization

*Computational field problems*, such as occur in computational fluid dynamics (CFD), electromagnetic field simulation, and essentially any investigation of a phenomenon whose physiology and physics can be modeled effectively by ordinary and/or partial differential equations, are frequently encountered



Fig. 35. Anisotropy creases near the corpus callosum. **Top left:** RGB map with fibers. **Top right:** Ridge surfaces. **Bottom left:** Valley surfaces. **Bottom right:** Valleys with fibers. From [114]

within biomedical computing. For this reason, visualization researchers have concentrated on developing effective ways to visualize large-scale computational fields. The output of such simulations might be a single field variable (such as voltage, pressure or velocity) or a combination of variables involving a number of scalar, vector, and/or tensor fields. However, much of current and previous visualization research has focused on methods and techniques for visualizing a single computational field variable (such as the extraction of an isosurface from a single scalar field). While visualizations of a single field are sometimes sufficient for the achievement of some biomedical research goals, effective simultaneous visualizations of multiple fields would greatly enhance many projects.

For this reason, biomedical computing is ripe for research in what we will term “multi-field” visualization[115], in which combinations of the above fields are visualized together to elucidate their *interactions*. The challenges for such multi-field visualizations are many and include large-scale data, complicated geometries, and heterogeneous and anisotropic material properties. Below are two examples of multi-field visualizations. Both examples illustrate the challenges involved in providing a researcher with intuitive and useful visual feedback.

In Figure 36, we give a simple example of a multi-field visualization from the

simulation of electric current flow within an anisotropic media. The sample volume has Dirichlet ( $\pm 1$  volts) boundary conditions on the opposite sides of the cube (orthogonal to the plane of view) and Neumann zero flux boundary conditions on all remaining sides. The media is described by a single conductivity tensor with all non-zero elements. The result is very unintuitive; the isosurfaces are not parallel to the sides of the cube and current lines are not orthogonal to these isosurfaces. Electric field lines will still be orthogonal to the isosurfaces, but will not be parallel to the sides of the cube.

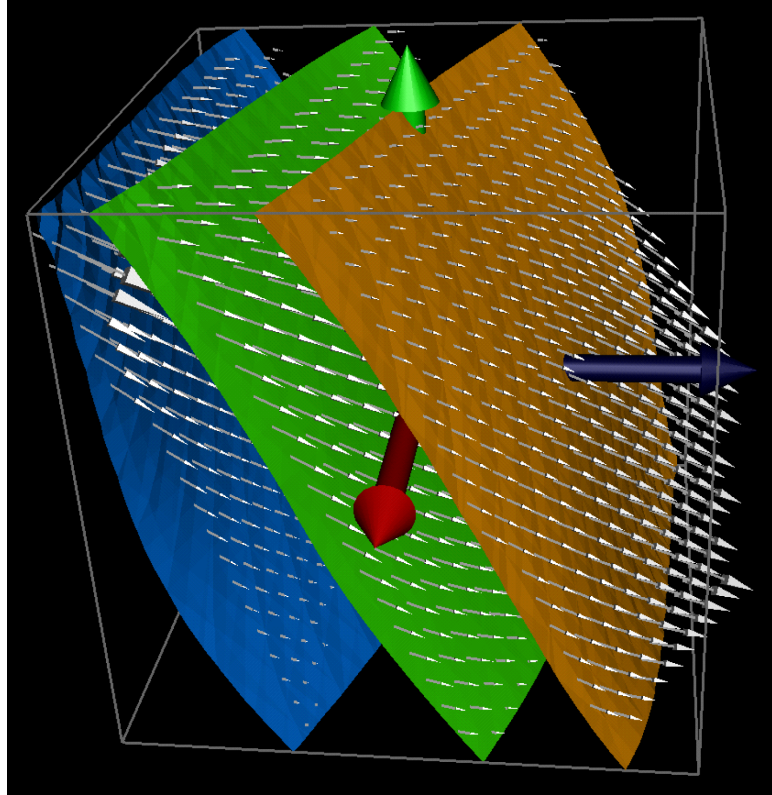


Fig. 36. Electric current flow within an anisotropic media. Note how current is not orthogonal to the isovoltage surfaces because of the anisotropic conductivity.

In another example of multi-field visualization, Figure 37, shows the results of a large-scale finite element simulation of the distribution of electric current flow and voltage within an inhomogeneous model of the human head and brain. The image shows a combination of an isovoltage surface and streamlines of current flow within the context of the magnetic resonance image scans and a geometric head model.

In the next figure 38 we see a multi-field visualization from a computational fluid flow simulation.

Another multi-field visualization idea is to use a combination of scalar and vector field visualization using glyphs for time-dependent data as shown in Figures (39 and 40), which illustrate the electrical potential along with the

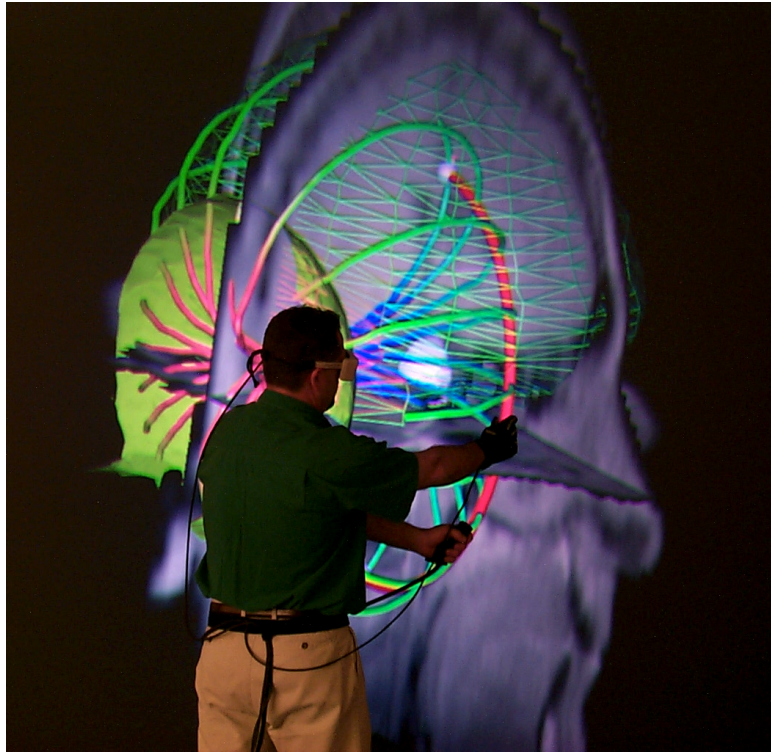


Fig. 37. Electric current flow within the brain arising from a localized source, visualized in an immersive environment.

current on the cardiac surface during excitation and repolarization, highlighting regions of in and outflow.

Another compelling example of the need and use of multi-field visualization arises from EEG inverse simulations. One of the open questions in inverse EEG source localization is what effect the anisotropy of white matter has on source localization accuracy. We applied a combination of stream surface visualization with simple tensor field visualization to look at the effects of including anisotropy within a realistic head model for the EEG source localization simulation. Figure 41 illustrates the effects of white matter anisotropy using these visualization techniques. We can observe a correlation between the primary direction of the conductivity structure of the white matter fiber bundles and the direction of the return currents. The visualization of return currents in bioelectric field problems can reveal important details about the distribution of sources, interactions at conductivity boundaries, and the effect of geometric distortion on bioelectric fields. By integrating the stream surfaces with a visualization of the diffusion tensors representing the white matter, we can better understand the relationship between structural, spatial relationships [116,117].

For generations, artists have attempted to convey complex and multiple ideas and images via limited channels. Painters, for example, use different brush

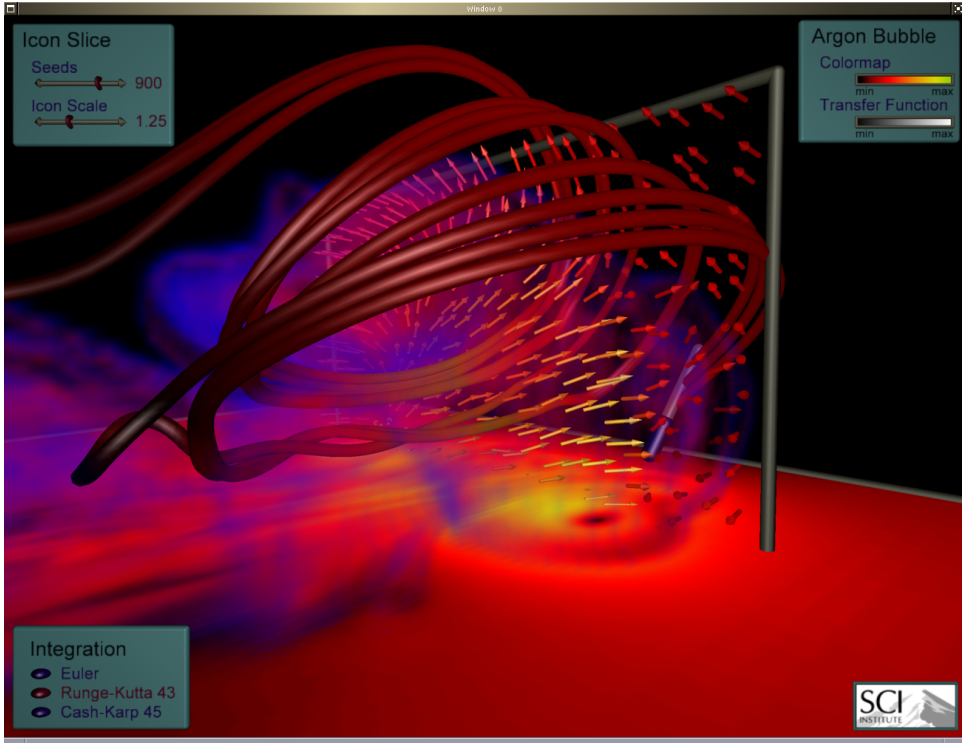


Fig. 38. This figure shows a multi-field visualization from a computational fluid flow simulation. Here we are visualizing two scalar fields by using volume rendering and the cutting plane in the x-y plane. We are also visualizing two vector fields using streamlines and arrows in the x-z cutting plane. Data courtesy of Lawrence Berkeley National Laboratory.

strokes and texture in layers to add depth and structure to oil paintings. In a similar way, we will employ creative methods to increase the number of channels that can be presented clearly in visualization. A successful example of the application of a painterly method applied to a scientific data set is shown in Figure 42. The authors, [118] use a combination of discrete and continuous visual elements arranged in multiple layers to represent the data and additional mathematically derived quantities such as derivatives or eigenvalues and eigenvectors of a diffusion tensor. Figure 42 shows a visualization of an airflow simulation based on this layered approach, which presents six different quantities in a compact way. In the bottom layer, the area of the ellipses represents divergence, while eccentricity encodes shear. The arrow layer conveys the velocity and speed via the direction and area, respectively, of the arrows. Finally, the ellipses encode the vorticity through their color, texture, and contrast..

These are just a few examples of our initial ideas and research in the emerging field of multi-field visualization. From a scientific perspective, multi-field visualization is valuable because it can generate novel hypotheses about the relationships between the underlying physical or biological quantities. Successful multi-field visualization requires visual transparency in all the constituent field

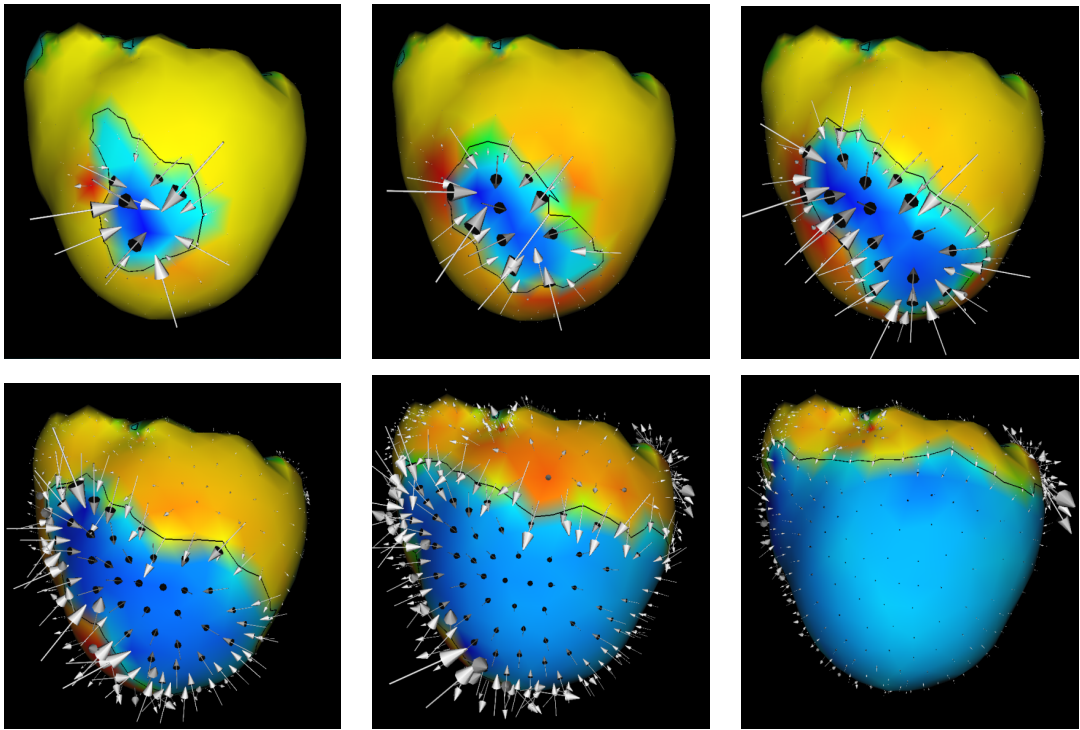


Fig. 39. Combined scalar and vector visualization I. The image shows the electrical potential and the electrical current over the cardiac surface during excitation, at 10 ms, 20 ms, 30 ms, 40 ms, 50 ms, and 60 ms respectively. The black lines indicate the boundary between regions of in and outflow of the electrical current. Data and image courtesy of Bruno Taccardi and Frank Sachse of the Cardiovascular Research and Training Institute.

visualizations. In the three-dimensional domains of biomedical researchers, it will be a challenge to generate such transparency, especially through techniques that are also intuitive and interactive.

## 5.2 Error and uncertainty visualization

With few exceptions, visualization research has ignored the visual representation of errors and uncertainty for three-dimensional visualizations. Certainly, this lack can be attributed partly to the inherent difficulty in defining, characterizing, and controlling comparisons between different data sets and partly to the corresponding error and uncertainty in the experimental, simulation, and/or visualization processes. In addition, visualization researchers have developed few methods that allow for easy comparison and representation of error and uncertainty in data for visualizations. To make current visualization techniques and software more useful to biomedical computing (and other) researchers, we need to incorporate visual representations of error and uncertainty [119].

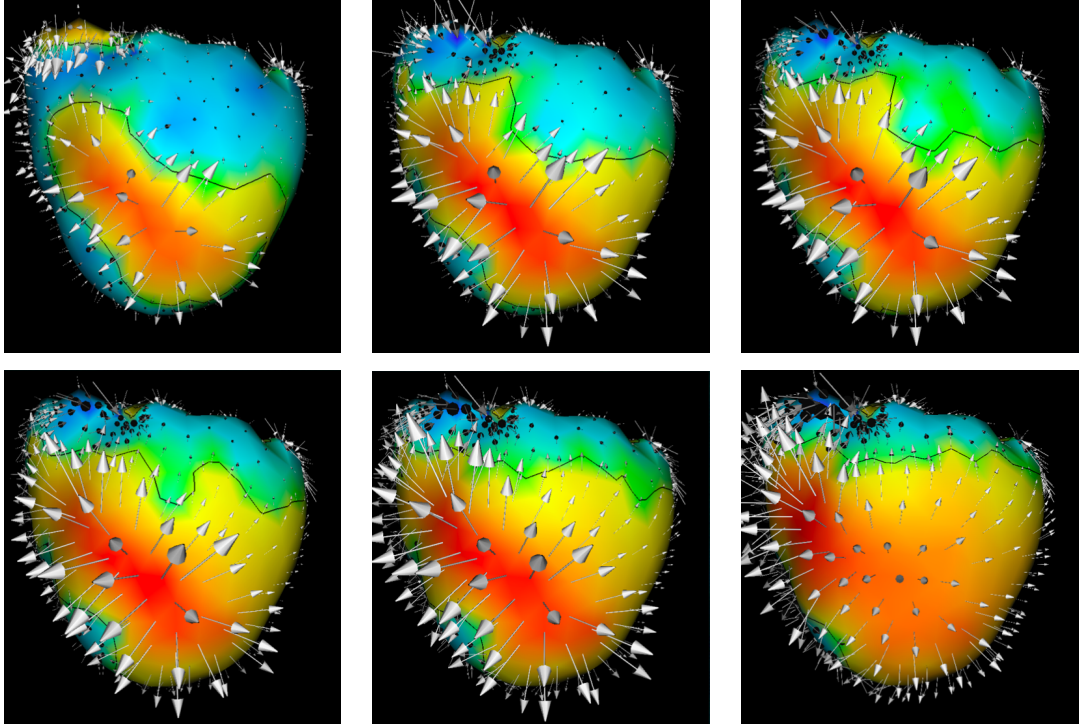
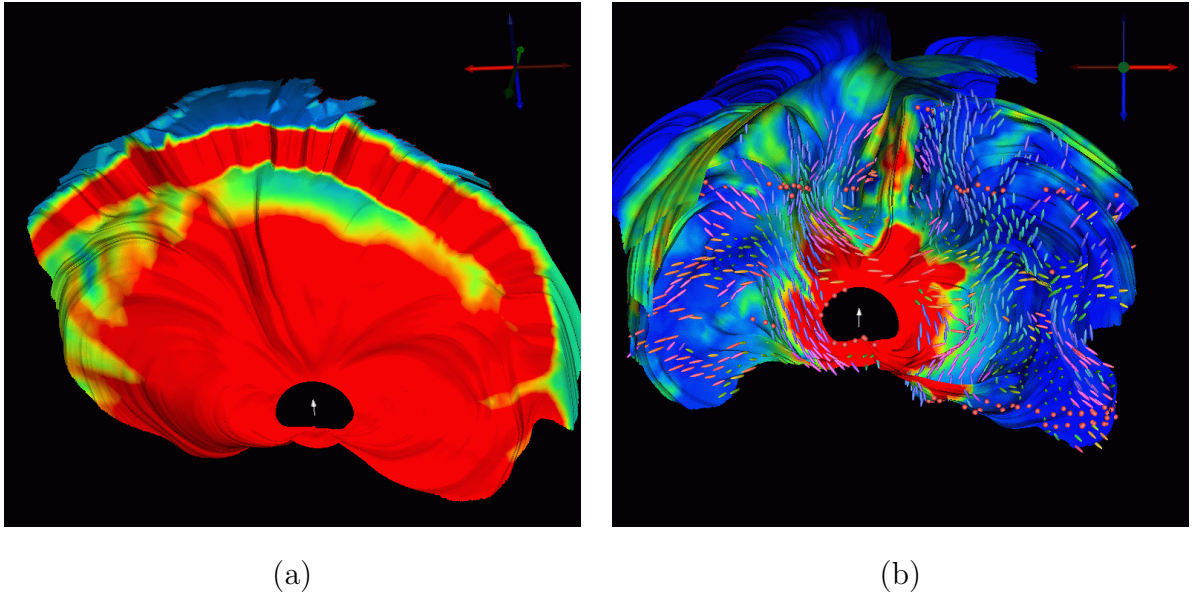


Fig. 40. Combined scalar and vector visualization II. Electrical potential and electrical current over the cardiac surface are shown during repolarization, at 110 ms, 130 ms, 150 ms, 170 ms, 190 ms, and 210 ms respectively. Data and image courtesy of Bruno Taccardi and Frank Sachse of the Cardiovascular Research and Training Institute.

A few visualization researchers have started thinking about how to create effective three-dimensional visual representations of errors and uncertainties, the sources of which can include uncertainty in acquisition (instrument measurement error, numerical analysis error, statistical variation), uncertainty in the model (both in mathematical and in geometric models), uncertainty in transformation (where errors may be introduced from resampling, filtering, quantization, rescaling), and uncertainty in visualization. (A useful overview of uncertainty definitions can be found in[120]). Pang et al.[121] have summarized a variety of techniques that might be used for uncertainty visualization. These techniques range from adding or modifying the geometry with, for example, a bump map or altered lighting attributes, to using textures. Perhaps the most interesting technique proposed is the use of blurring, as shown in Figure 43. Grigoryan et al.[122], on the other hand, used point-based primitives instead of blurring to create a fuzzy surface that achieves similar results, Figure 44. Blurring is a natural cue to the eye that something is amiss. This technique can easily be applied to a variety of different visualization techniques from particle tracing to isosurfacing, as we describe later on.

Our reaction-diffusion visualization technique described in section 3.4 can be modified to create a way to represent uncertainty in the vector field. By al-



(a)

(b)

Fig. 41. Visualization of return current surfaces from an EEG simulation using a deep thalamic source. The two visualizations show the results of the simulation using an isotropic model (a) and a model including anisotropic white matter (b).

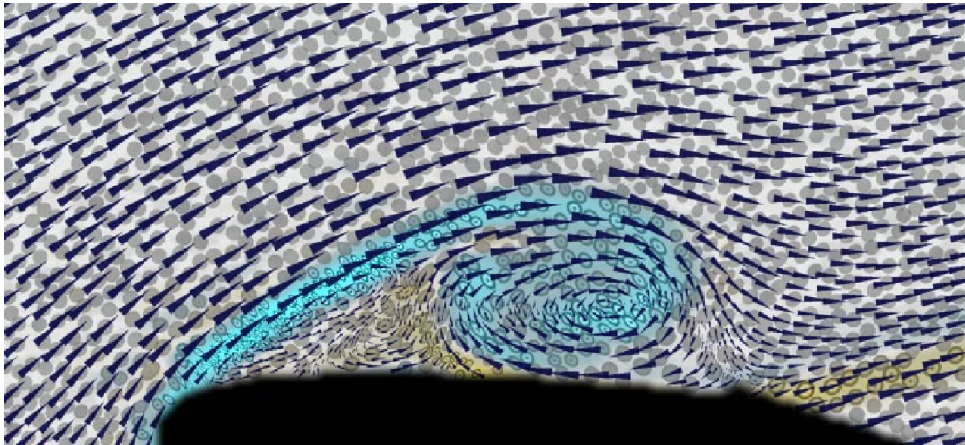


Fig. 42. Visualization of experimental two-dimensional flow past an airfoil, indicating velocity, speed, vorticity, rate of strain, divergence, and shear. Image courtesy R.M. Kirby and H. Marmanis and D.H. Laidlaw.

lowing the amount of anisotropy in the reaction-diffusion model to vary, we embed another variable that can be visually mapped and controlled. For example, let us assume that we have a uncertainty in the vector field associated with orientation. We can use the anisotropy tensor within the reaction diffusion equation to help create a visual mapping of uncertainty to the resulting spot pattern. When the amount of anisotropy within the reaction diffusion equation is small (corresponding to a high value of uncertainty), we can cause the spot to take an almost circular shape, with the ratio of the semi-axes being approximately one. However, when the anisotropy within the reaction diffusion equation is high (corresponding to a low value of uncertainty), we can

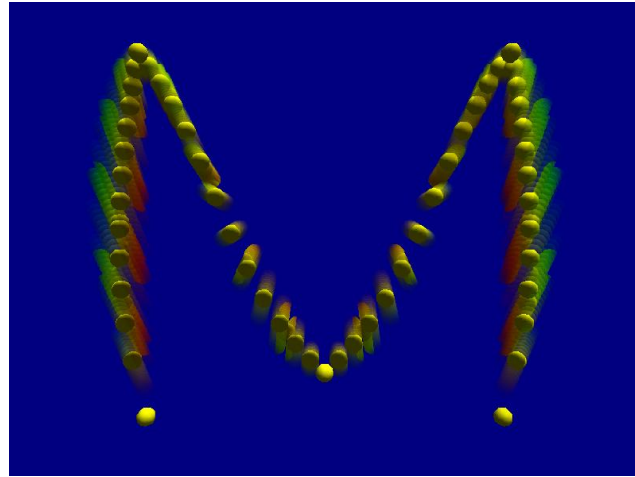


Fig. 43. Particle tracing using blurring to show the uncertainty in the path. Used with permission of the author.

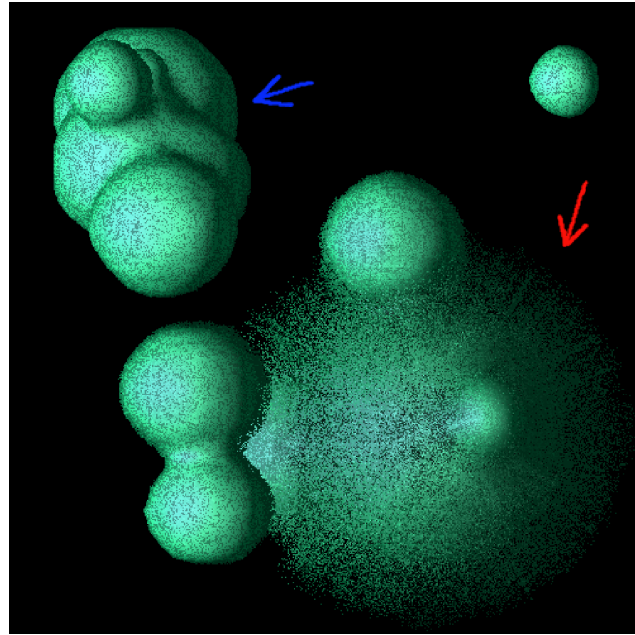


Fig. 44. Point-based primitives used to create a fuzzy surface to show uncertainty. Used with permission of the author.

cause the spot to take the shape of an ellipse, deforming at times so extremely that it appears almost as a thick line *i.e.*, the ratio of the semi-axes becomes very large. This creates a visual difference very well suited to mapping an orientation uncertainty. When the orientation uncertainty is very small, the spot is elliptical, reflecting a precise orientation. When the uncertainty is very high, the spot is more circular, reflecting the uncertainty in the orientation. This is demonstrated in Figure 45 on a synthetic circular field where the uncertainty in the direction is a function of the angle [123,69].

One simple example of the error and uncertainty visualization techniques com-

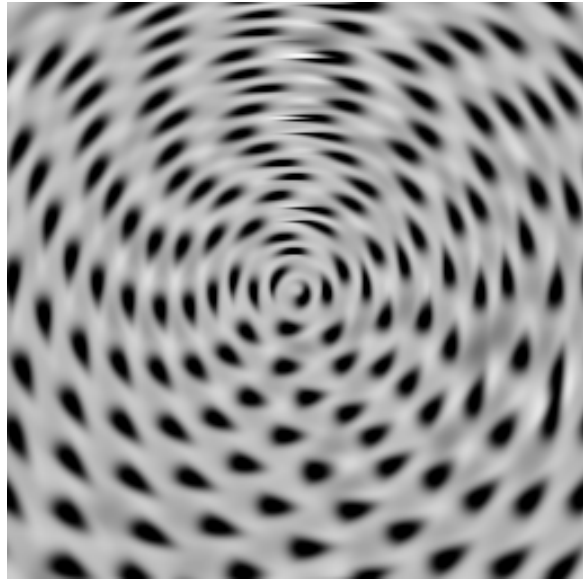


Fig. 45. Reaction diffusion vector field model visualization of orientation uncertainty. A more elliptical pattern represents low orientation uncertainty, while a more circular pattern represents a higher uncertainty in the orientation of the vector field.

combines isosurface methods with volume rendering methods. For example, one can represent the average value of a scalar field with an isosurface and then represent the error or uncertainty of the scalar field using volume rendering, as shown in Figures 46 and 47.

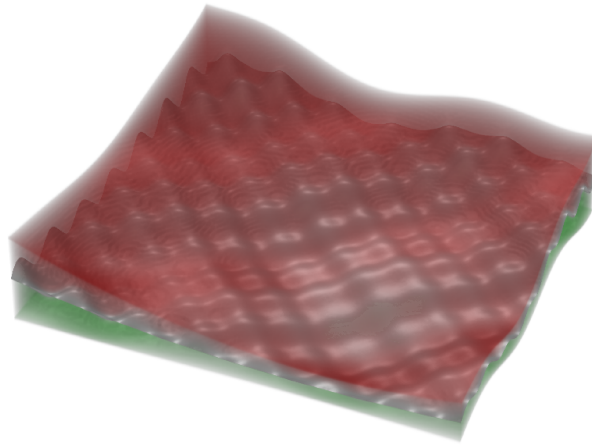


Fig. 46. An isosurface of a synthetic dataset (in gray) is bracketed with volume-rendered regions (red and green) indicating uncertainty around the isovalue.

Most recently we have proposed an alternative approach to encoding uncertainty in volume rendering visualizations [124]. Our method offers an intuitive



Fig. 47. An isosurface of an MRI dataset (in orange) is surrounded by a volume-rendered region of low opacity (in green) to indicate uncertainty in surface position.

means to interactively select the transfer function for a precomputed fuzzy classified volume data. One key feature of this new method is to permit the manipulation of the transfer function directly in the feature space. The user can therefore interact with the visualization at a semantic level. Moreover the uncertainty present in the fuzzy classification as a result of the mixture of neighboring material intensities at each sample point can be properly integrated in the volume rendering representation to draw user attention to the lack of a clear-cut boundary between homogeneous materials. The benefits of this approach are illustrated in Figure 48.

## 6 Information Visualization

## 7 Visualization Software

The are a variety of commercially available and research-based general visualization systems that may be useful for biomedical visualization (see [4] for an overview of visualization systems). While certainly not an exhaustive list, examples of these systems are:

**Amira:** Amira is a professional image segmentation, reconstruction, and 3d model generation application produced by Mercury Computer Systems GmbH ([www.amiravis.com](http://www.amiravis.com)). It is used by research and development groups

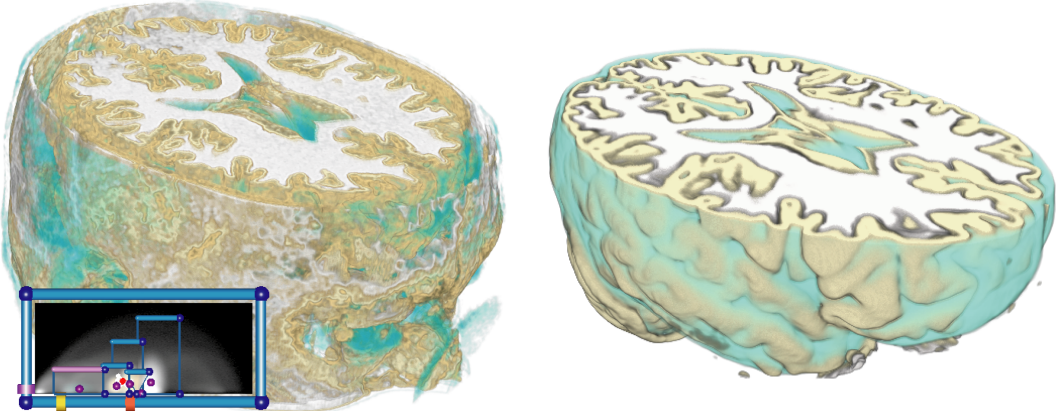


Fig. 48. A Comparison of transfer function-based classification versus data-specific probabilistic classification. Both images are based on T1 MRI scans of a human head and show fuzzy classified white matter, gray matter, and cerebro-spinal fluid from [124]. **Left:** Results of classification using a carefully designed 2D transfer function based on data value and gradient magnitude. **Right:** Visualization of the data classified using a fully automatic, atlas-based method that infers class statistics using minimum entropy, non-parametric density estimation [125].

in chemistry, biology, medicine, material science, etc. Amira is designed to handle confocal microscopy, MRI, or CT data. It uses the tcl language as a command interface for scripting and is built on top of the OpenGL and Open Inventor toolkits. Modules can be developed to extend the Amira system and can use parallelization techniques if the developer so desires.

**IDL:** Research Systems Inc.'s Interactive Data Language (IDL) ([www.rsinc.com/idl](http://www.rsinc.com/idl)) is used for data analysis and visualization and to rapidly develop algorithms and interfaces. IDL is a 'Matlab'-like tool that interprets the commands entered by the user.

**MicroView:** MicroView is an open-source, freely-distributed 3D volume viewer. It is written in Python and uses VTK for its graphical capabilities.

**OsiriX:** OsiriX is an open-source image processing software package dedicated to DICOM images produced by medical equipment (MRI, CT, PET, PET-CT, etc) and confocal microscopy designed to run under OSX on the Mac. It offers many visualization modes including surface and volume rendering for 2D and 3D interrogation of the data. It is multi-threaded, and takes advantage of graphic board acceleration.

**VTK:** VTK, The Visualization Toolkit ([www.kitware.com](http://www.kitware.com)), is a public domain visualization package that is widely used in both classroom settings and research labs. It provides general visualization capabilities for scalars, vectors, tensors, textures, and volumetric data. Written in C++, VTK includes Tcl, Python and Java bindings for application development and prototyping. VTK contains some built-in parallelization pieces for both thread-

ing and MPI.

**AVS:** Advanced Visual Systems' ([www.avx.com](http://www.avx.com)) AVS was the first commercially available dataflow visualization system. AVS/Express provides general visualization capabilities for scalar and vector visualization. The Manchester England AVS Center provides user contributed models that add functionality to the commercial system. AVS/Express allows for C++/C/Fortran legacy codes to be integrated using a modular approach.

**IBM Open Visualization Data Explorer:** IBM Open Visualization Data Explorer, OpenDX

([www.research.ibm.com/dx](http://www.research.ibm.com/dx)), is a public domain dataflow visualization system similar to AVS/Express. OpenDX as it is a community-based open software project.

**Iris Explorer:** Iris Explorer ([www.nag.com](http://www.nag.com)) is another commercially-available dataflow visualization system. The newest version allows modules to be optionally (off-line) compiled into a single executable. This allows the user to run the group as a single process thus using less CPU time and memory than required by the original separate modules. Individual modules may be written to use parallel processing, but this is not directly facilitated by Iris Explorer.

**ANALYZE:** The ANALYZE software system (developed at the Mayo Clinic) is a comprehensive commercially available software packages for three-dimensional biomedical image visualization and analysis.

In this next section, we describe open source visualization software tools that have been developed at the SCI Institute.

## 7.1 *SCIRun/BioPSE visualization tools*

The SCIRun system has been a focus of research and development at the SCI Institute since 1995[126,127]. Its framework for visualization, modeling, and simulation has been the test bed for much of our fundamental research in visualization techniques and their applications to real-world scientific problems. As such, it supports all the standard techniques of scientific visualization and our improvements upon them. This includes efficient extraction of iso-surfaces (unstructured and structured grids) and volume rendering of scalar fields, streamlines and hedge-hogs for vector fields, as well as of tensorlines and glyphs for tensor fields. The visualization can be interactively created and modified with data probe widgets located within the field geometry. In 2000, the SCIRun PSE (*Problem Solving Environment*) was made available to the research community as open source software[128].

We show an example of the SCIRun/BioPSE software system for an electroencephalography (EEG) source localization application in Figures 49 and

50. Figure 49 contains the dataflow network that implements an inverse EEG application. At the top of the network, the input data files are loaded; these include the finite element mesh that defines the geometry and conductivity properties of the model and a precomputed lead-field matrix that encodes the relationship between electric sources in the domain and the resulting potentials that would be measured at the electrodes. Further down in the network, we have a set of modules that optimize the dipole location in order to minimize the misfit between the measured potentials from the electrodes and the simulated potentials due to the dipole. Finally, we have visualization and rendering modules, which provide interactive feedback to the user.

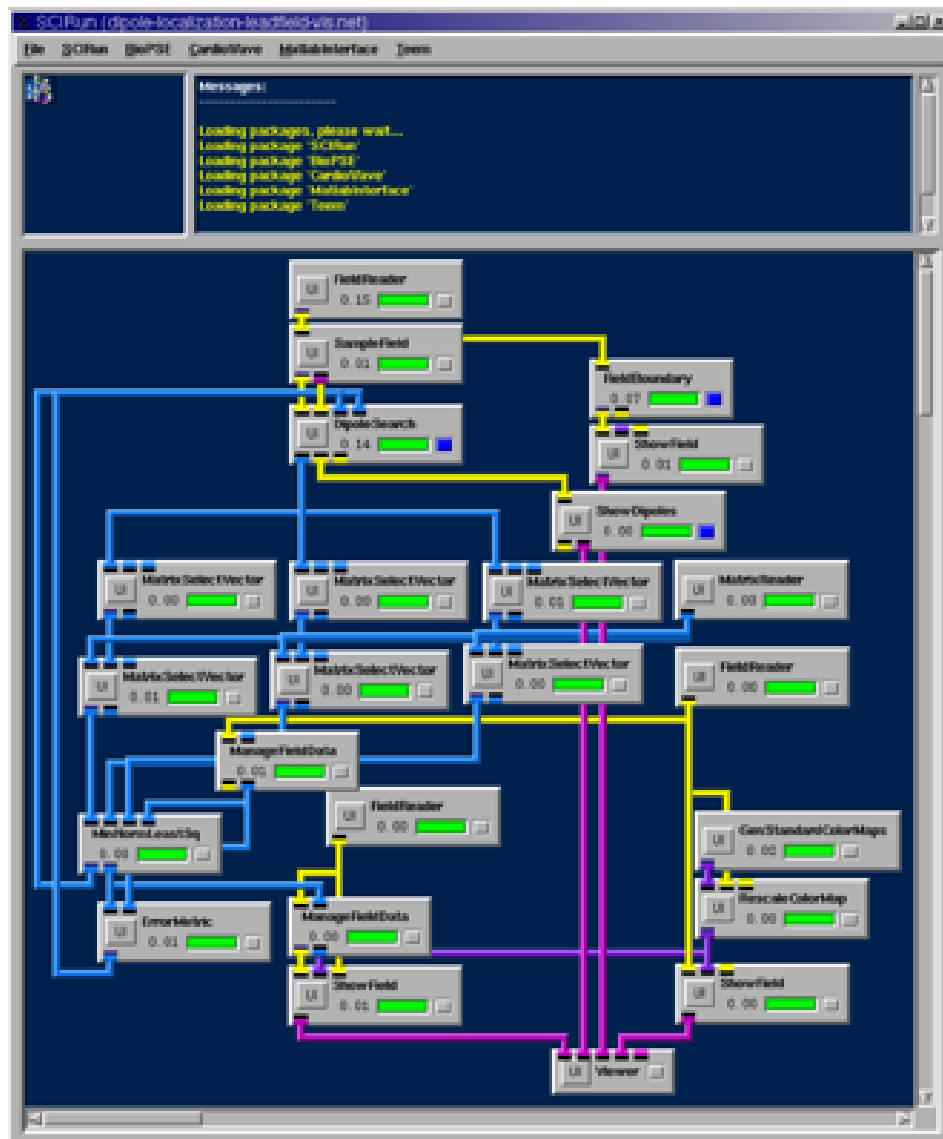


Fig. 49. SCIRun/BioPSE modules combined for EEG modeling (unstructured mesh generation), simulation (finite element simulation, parallel linear system solves, and inverse source localization), and visualization (mesh visualization, isosurface extraction, and vector field visualization).

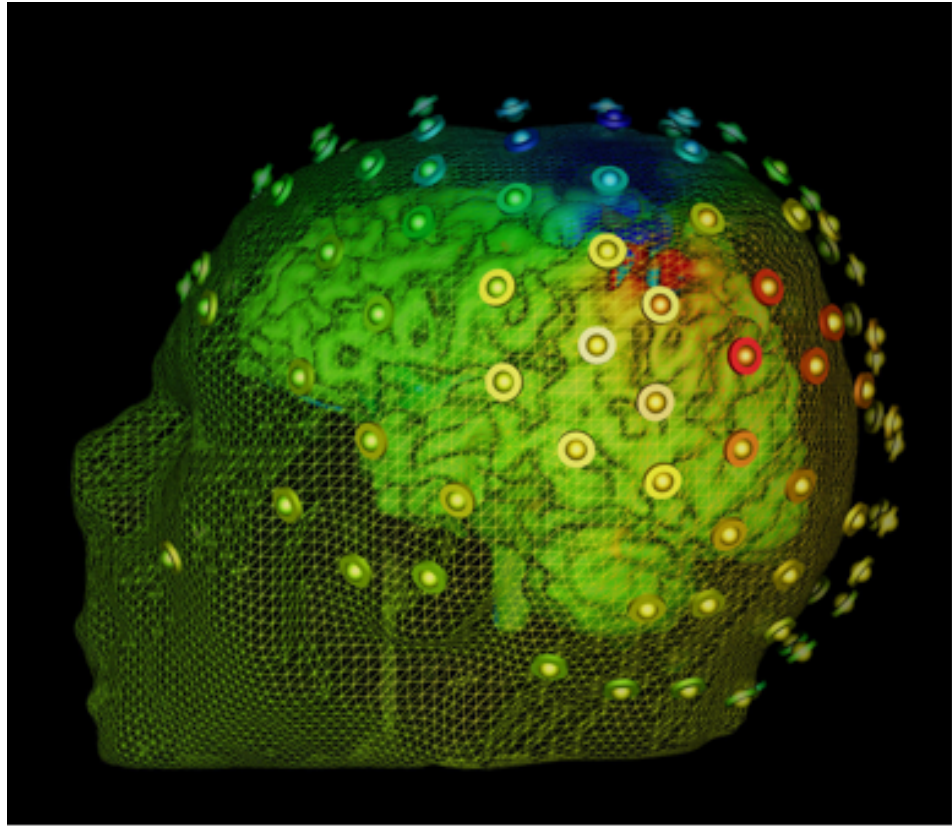


Fig. 50. Visualization of simulation results of an EEG simulation localizing a neural source.

#### 7.1.1 *SCIRun PowerApps*

One of the major hurdles to SCIRun becoming a practical tool for the scientists and engineers has been SCIRun’s dataflow interface. While visual programming is natural for computer scientists and some engineers, who are accustomed to writing software and building algorithmic pipelines, it is sometimes overly cumbersome for application scientists . Even when a dataflow network implements a specific application (such as the bioelectric field simulation network provided with BioPSE and detailed in the BioPSE Tutorial), the user interface (UI) components of the network are presented to the user in separate UI windows, without any semantic context for their settings. For example, SCIRun provides file browser user interfaces for reading in data. However, on the dataflow network all of the file browsers have the same generic presentation. Historically, there has not been a way to present the filename entries in their semantic context, for example to indicate that one entry should identify the electrodes input file and another should identify the finite element mesh file. While this interface shortcoming has long been identified, it has only recently been addressed. With a recent release of BioPSE/SCIRun, we introduced PowerApps. A PowerApp is a customized interface built atop a dataflow application network. The dataflow network controls the execution

and synchronization of the modules that comprise the application, but the generic user interface windows are replaced with entries that are placed in the context of a single application-specific interface window. A comparison of the dataflow version and the PowerApp version is shown in Figures 51 and 52.

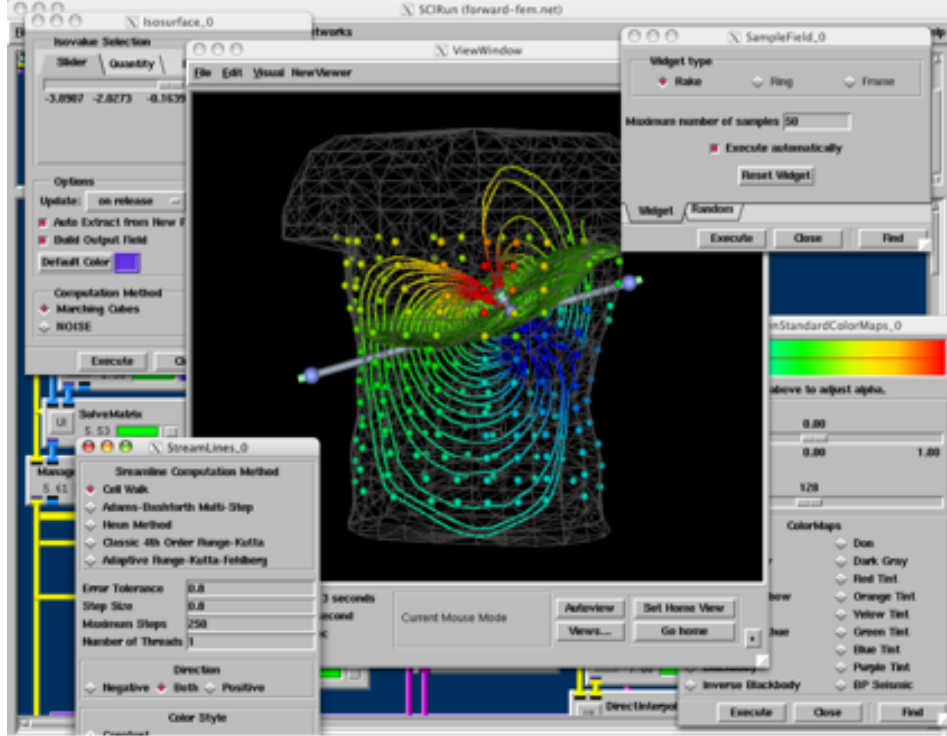


Fig. 51. BioPSE dataflow interface for a bioelectric field application.

## 7.2 *map3d*

A special area of visualization that arises in many biomedical domains is displaying sets of time signals that represent scalar values at numerous locations in space. Examples come from electrophysiology of the heart [129–137] and nervous system[138–140] and many others in which scientists and engineers deal with high spatial and temporal resolution of their measured or simulated data. The challenges of this form of visualization include representing both geometric shape and the associated data in a manner that is clear to the user, establishing quantitative, flexible coding and scaling of the data for detailed interactive analysis, and preserving efficiency so that a user may sort through very large (tens to hundreds of MBytes) data sets.

One approach to these visualization goals is *map3d*, an open-source software project that has been developed over the past 10 years for use in a wide range of applications in biomedical research[129,130,132]. *map3d* is written using the OpenGL standard graphics library and there are versions for all the major

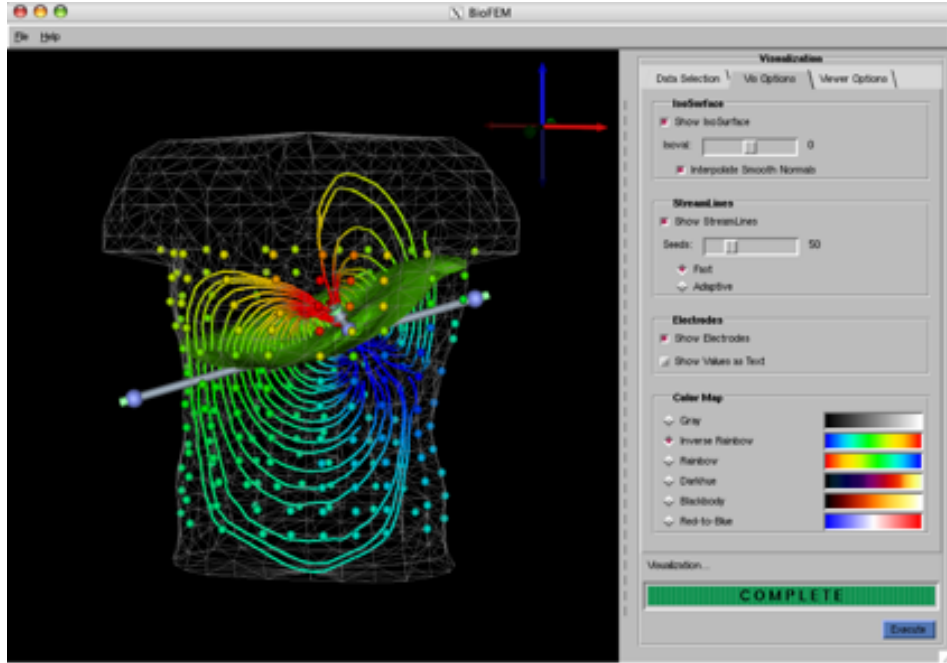


Fig. 52. The BioFEM PowerApp custom interface. Though the application is functionality equivalent to the dataflow version shown in Figure 51, this PowerApp version provides an easier-to-use custom interface. Everything is contained within a single window; the user is lead through the steps of loading and visualizing the data with the tabs on the right; and generic control settings have been replaced with contextually appropriate labels; and application-specific tooltips (not shown) appear when the user places the cursor over any user interface element.

platforms (Windows, MacOSX, Linux, SGI Irix). The motivating application for *map3d* was visualizing results from simulations and experiments in cardiac electrophysiology of the whole heart and although this remains the dominant application, it has also found use for displaying skin temperature profiles, scalp electric potentials from electroencephalography, and even concentration profiles in the nephrons of the kidney. More generally, *map3d* contains elements and capabilities that are typical of other solutions to the need to view this type of data.

The essential structure of *map3d* is a set of locations in space (nodes), usually connected to form surfaces of triangles and time signals associated with each of these nodes. The user must identify the nodes and may use *map3d* to connect them and must provide some form of mapping between channels of time signal and the nodes. From this information, *map3d* provides a highly interactive environment with which to view multiple sets of data associated with the same or multiple sets of nodes/triangles.

To illustrate *map3d* functionality, Figure 53 shows an example of potentials recorded from the surface of a dog heart using a 600-electrode sock array. The figure also shows the capability to display not just scalar values from

time series but also quantities derived from those time series. In the figure, the center image contains what is known as the “activation” time, *i.e.*, the time instant at which the cardiac wave of excitation passes each location. The specific case in Figure 53 shows a heart beat that initiated in the center of the ventricles, indicated by the smallest concentric ellipse colored dark blue in the image. Contours here indicate discrete values of activation time, spaced at 5-millisecond intervals, and show the pathway of a single activation sequence (*i.e.*, the electrical sequence that leads to the contraction phase of the heart beat). The surrounding maps contain renderings of electric potential at a sequence of time instants, as indicated by the red vertical bar on the time signal below each frame. *map3d* offers the capability of rendering not only the activation time in its own window but also the activation contour that corresponds to each instant in time within the potential maps—the arrows in the figure indicate the relationship between the activation time and the thick red band in each of the four potential maps corresponding to 312, 316, 320, and 324 ms, respectively from the start of the measurement. This figure also shows the unique support *map3d* provides for displaying visual queues or “landmarks”, in this case the red tubes lying on the surface of the heart that show the location of the coronary arteries.

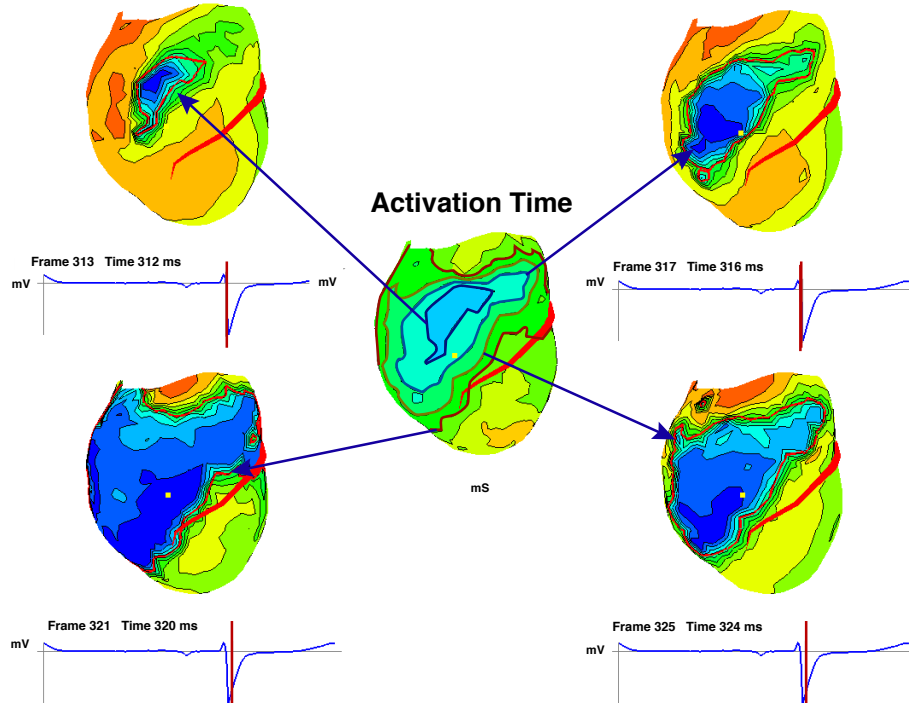


Fig. 53. Example of *map3d* visualization of cardiac potentials and activation times.

The importance of this type of visualization lies in its ability to incorporate

multiple information sources of quite different nature into the same visualization. There are many quantities one can derive from bioelectric time signals that have meaning on their own, just as activation time provides a compact representation of the trajectory of the excitation wave in the heart. The challenge becomes then to display this mixed information in a way that is intuitive and simple for the user. *map3d* now supports complex file formats that contain all the information derived from a set of time signals as well as the time signals themselves so that once constructed (the task of other programs), the user can quickly evaluate a large volume of information with *map3d*.

Another example of *map3d* visualization of multiple data sources is shown in Figure 54, which contains a sequence of electric potential maps recorded from the outer surface (epicardium) and inner surface (left-ventricular endocardium) of a canine heart. *map3d* offers many options for quantitative examination of data sets such as this including the ability to select any point in the surface rendering and see the associated time signal; an enormous array of scaling options, including dynamically coupling the scaling across multiple surfaces; selecting new reference signals (important in evaluating EEG data); and even marking of data values directly on the surface.

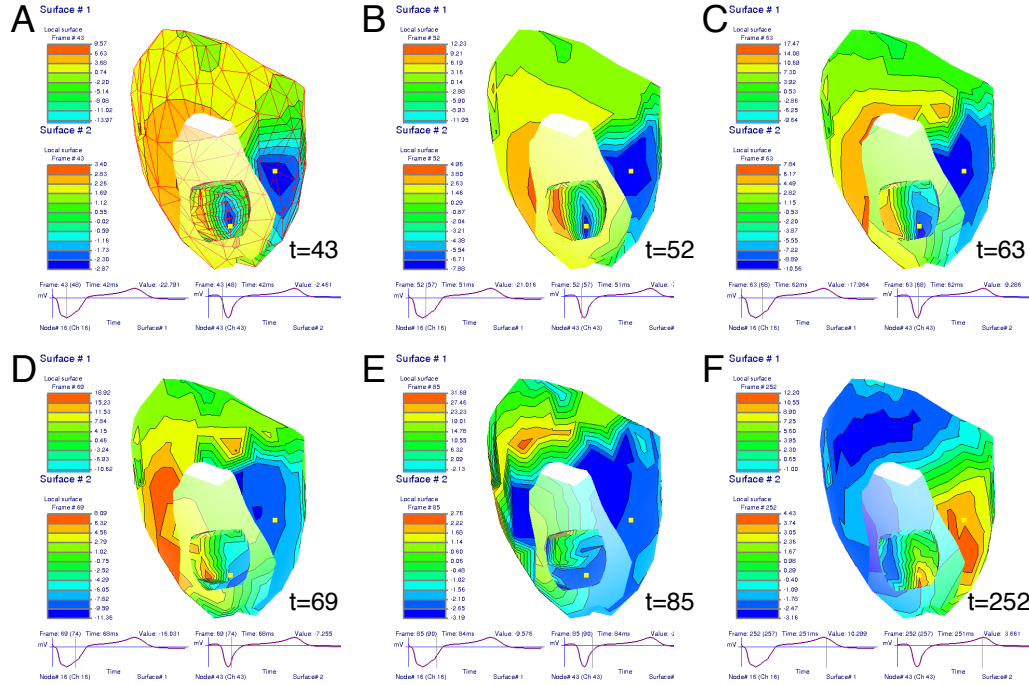


Fig. 54. Sequence of potentials from the outer and inner surfaces of the heart. Image show the use of clipping planes to reveal data from two concentric surfaces simultaneously. The first image in the sequence shows the underlying measurement meshes for both surfaces (in red) and the time values marked in each panel indicate the time after stimulation of the heart from the epicardium.

A final example of *map3d* functionality that provides additional visual references is shown in Figure 55. Here the entire display of geometry, potentials,

time signals, and scaling bars is superimposed over a related image of the source of the data. The user can manually scale and align the geometry or prescribe the parameters for consistent alignment across multiple instances of the program.

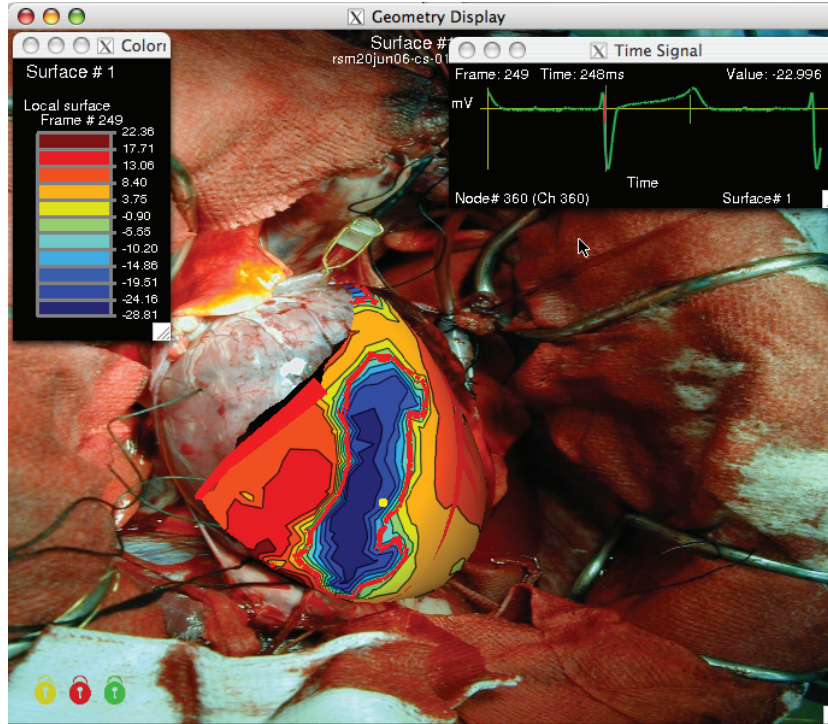


Fig. 55. Visualization of data from the surface of the heart superimposed on an image of the same heart during the experiment. Color coding is for surface potentials with the think red contour indicating the location of activation. The time signal in the upper right corner of the figure shows a vertical red mark indicating the time instant captured in the surface map.

**7.2.0.1 Application domains of *map3d*** Typical applications of *map3d*—and the origins of the program—are in mapping the spatial and temporal features of cardiac electrophysiology and for this purpose there remains, to our knowledge, no suitable alternative. Other application areas require the same basic functionality, *i.e.*, whenever there exist time signals associated with locations on a surface in three-dimensional space, there are similar set of visualization needs. Some examples from biomedicine include bioelectric signals from the head, skeletal muscle, or even the eye. However, one might also visualize temperature variations over the surface of the body or even the distribution of RNA expression over a two-dimensional tissue preparation.

## 8 Summary and Conclusion

New imaging modalities, more accurate simulation models, and continued growth in computational power all contribute to confronting biomedical researchers and engineers with an unprecedented volume of information to further their understanding of biological systems and improve clinical practice. As the size and complexity of the resulting data explode, the tools created by Scientific Visualization research become crucial to gaining insight into the underlying biophysical phenomena. In this chapter, we have offered a selected overview of recent advances in biomedical visualization, while emphasizing promising avenues for future research.

Following a natural decomposition, techniques were presented that address the specific challenges posed by the exploration and analysis of large-scale scalar, vector, and tensor biophysical datasets. We showed that, in each case, both effective general purpose and application specific methods have been devised by the Scientific Visualization community over the last decade. The proposed algorithms address the need for effective visual representations while ensuring an efficient processing of large data that supports user interaction. We also discussed the question of the depiction of the error and uncertainty present in the visualization pipeline. While the importance of this aspect has long been underestimated, it is now regarded as an essential component of a useful visual analysis within a scientific study. We concluded our presentation with an overview of some of the existing visualization software packages that feature the methods that we discussed. In particular we gave a more detailed description of *BioPSE* and *map3d* that the Scientific Computing and Imaging Institute has developed and made publicly available for the benefit of the biomedical community.

Finally, we would like to mention two important additional visualization research areas that we did not cover in this chapter that could have entire chapters devoted to them. Information visualization is an active research field concerned with the visual representation of abstract data with no natural spatial embedding. For example, it provides compelling tools to support analysis in bioinformatics [141,142]. Another biomedical visualization area that has received a significant interest over the last few years is molecular visualization [143–146].

## 9 Acknowledgments

The authors would like to thank the many people who contributed to this article including: Charles Hansen, Gordon Kindlmann, Joe Kniss, Rob MacLeod,

Steve Parker, C.F. Westin, Ross Whitaker, and Leonid Zhukov. The authors would like to acknowledge support from NIH NCRR Grant P41-RR12553-07, and additional support from NIH, NSF, and DOE.

## References

- [1] C.R. Johnson, R. Moorhead, T. Munzner, H. Pfister, P. Rheingans, and T. S. Yoo. NIH-NSF Visualization Research Challenges Report, 2006. <http://tab.computer.org/vgtc/vrc/index.html>.
- [2] 2007. Scientific Computing and Imaging Institute (SCI), University of Utah, [www.sci.utah.edu](http://www.sci.utah.edu).
- [3] W. Schroeder, K. Martin, and B. Lorensen. *The Visualization Toolkit: An Object Oriented Approach to Graphics*, chapter 6. Kitware, Inc., Clifton Park, New York, 2003.
- [4] C.D. Hansen and C.R. Johnson. *The Visualization Handbook*. Elsevier, 2005.
- [5] Vidya Elangovan and Ross T. Whitaker. From sinograms to surfaces: A direct approach to the segmentation of tomographic data. In *Proceedings of the 4th Int. Conf. Medical Image Computing and Computer-Assisted Intervention*, pages 213–223. Springer-Verlag, 2001.
- [6] J. Kniss, G. Kindlmann, and C. Hansen. Multidimensional transfer functions for interactive volume rendering. 8(3):270–285, 2002.
- [7] J.M. Kniss, S. Premoze, M. Ikits, A. E. Lefohn, C.D. Hansen, and E. Praun. Gaussian transfer functions for multi-field volume visualization. In *IEEE Visualization 2003*, pages 497–504, October 2003.
- [8] G. Kindlmann, R. Whitaker, T. Tasdizen, and T. Möller. Curvature-based transfer functions for direct volume rendering: Methods and applications. In *Proceedings Visualization 2003*, page 67, October 2003.
- [9] M. Ikits, J.M. Kniss, A.E. Lefohn, and C. Hansen. Volume rendering techniques. In Randima Fernando, editor, *GPU Gems: Programming Techniques, Tips and Tricks for Real-Time Graphics*, page (to appear). Addison Wesley, 2004.
- [10] J.M. Kniss, J.P. Schulze, U. Wossner, P. Winkler, U. Lang, and C.D. Hansen. Medical applications of multi-field volume rendering. page (Accepted), 2004.
- [11] J.M. Kniss, S. Premoze, C. Hansen, and D. Ebert. Interactive translucent volume rendering and procedural modeling. 2002.
- [12] J. Kniss, P. McCormick, A. McPherson, J. Ahrens, J. Painter, A. Keahey, and C. Hansen. Interactive texture-based volume rendering for large datasets. 21(4):52–61, July/August 2001.

- [13] J.M. Kniss, P. McCormick, A. McPherson, J. Ahrens, J. Painter, A. Keahey, and C.D. Hansen. T-rex, texture-based volume rendering for extremely large datasets. 21(4):52–61, 2001.
- [14] G.L. Kindlmann, D.M. Weinstein, and D. Hart. Strategies for direct volume rendering of diffusion tensor fields. 6(2):124–138, April-June 2000.
- [15] G. Kindlmann and J. Durkin. Semi-automatic generation of transfer functions for direct volume rendering. In *IEEE Symposium on Volume Visualization*, pages 79–86. IEEE Press, Oct 1998.
- [16] J.M. Kniss, G. Kindlmann, and C.D. Hansen. Multidimensional transfer functions for volume rendering. In C.D. Hansen and C.R. Johnson, editors, *The Visualization Handbook*, pages 189–210. Elsevier, 2005.
- [17] J. Kniss, G. Kindlmann, and C. Hansen. Interactive volume rendering using multi-dimensional transfer functions and direct manipulation widgets. pages 255–262, October 2001.
- [18] 2007. BioPSE: Problem Solving Environment for modeling, simulation, image processing, and visualization for biomedical computing applications. Scientific Computing and Imaging Institute (SCI), Download from: <http://www.sci.utah.edu/cibc/software/>.
- [19] W.E. Lorensen and H.E. Cline. Marching cubes: A high resolution 3D surface construction algorithm. *Computer Graphics*, 21(4):163–169, 1987.
- [20] Geoff Wyvill, Craig McPheeers, and Brian Wyvill. Data structure for soft objects. *The Visual Computer*, 2:227–234, 1986.
- [21] R.S. Gallagher. Span filter: An optimization scheme for volume visualization of large finite element models. In *Proceedings of Visualization '91*, pages 68–75. IEEE Computer Society Press, Los Alamitos, CA, 1991.
- [22] T. Itoh, Y. Yamaguchi, and K. Kooyamada. Volume thining for automatic isosurface propagation. In *Visualization '96*, pages 303–310. IEEE Computer Society Press, Los Alamitos, CA, 1996.
- [23] J.S. Painter, P. Bunge, and Y. Livnat. Case study: Mantle convection visualization on the cray t3D. In *Visualization '96*, pages 409–412. IEEE Computer Society Press, Los Alamitos, CA, 1996.
- [24] H. Shen and C. R. Johnson. Sweeping simplices: A fast iso-surface extraction algorithm for unstructured grids. *Proceedings of Visualization '95*, pages 143–150, 1995.
- [25] H.W. Shen, C.D. Hansen, Y. Livnat, and C.R. Johnson. Isosurfacing in span space with utmost efficiency (ISSUE). In *Visualization '96*, pages 287–294. IEEE Press, 1996.
- [26] Y. Livnat, H. Shen, and C.R. Johnson. A near optimal isosurface extraction algorithm using the span space. *IEEE Trans. Vis. Comp. Graphics*, 2(1):73–84, 1996.

- [27] P. Cignoni, C. Montani, E. Puppo, and R. Scopigno. Optimal isosurface extraction from irregular volume data. In *Proceedings of IEEE 1996 Symposium on Volume Visualization*. ACM Press, 1996.
- [28] C.L. Bajaj, V. Pascucci, and D.R. Schikore. Fast isocontouring for improved interactivity. In *Proceedings of 1996 Symposium on Volume Visualization*, pages 39–46, 1996.
- [29] C.L. Bajaj, V. Pascucci, and D.R. Schikore. The contour spectrum. In *Proceedings IEEE Visualization 1997*, pages 167–173, 1997.
- [30] Y. Livnat, C.D. Hansen, S.G. Parker, and C.R. Johnson. Isosurface extraction for large-scale datasets. In F. Post, editor, *Proceedings of Scientific Visualization -Dagstuhl‘2000*, 2001.
- [31] Y. Livnat, X. Cavin, and C. Hansen. PHASE: Progressive hardware assisted isosurface extraction framework. SCI Institute Technical Report UUSCI-2002-001, University of Utah, 2002.
- [32] Y. Livnat and C. Hansen. Dynamic view dependent isosurface extraction. SCI Institute Technical Report UUSCI-2003-004, University of Utah, 2003.
- [33] Y. Livnat and X. Tricoche. Interactive point based isosurface extraction. pages 457–464, 2004.
- [34] H. W. Shen and C.R. Johnson. Differential volume rendering: A fast algorithm for scalar field animation. In *Visualization 94*, pages 180–187. IEEE Press, 1994.
- [35] R Yagel and A. Kaufman. Template-based volume viewing. In *Proceedings of EUROGRAPHICS ’92*, volume 11, pages 153–157. Blackwell, Cambridge, England, September 1992.
- [36] R Yagel and Z. Shi. Accelerating volume animation by space-leaping. In *Proceedings of Visualization ’91*, pages 62–69. IEEE Computer Society Press, Los Alamitos, CA, October 1993.
- [37] K.L. Ma, J. Painter, C. Hansen, and M. Krogh. Parallel volume rendering using binary-swap compositing. *IEEE Computer Graphics and Applications*, 14(4):59–68, 1994.
- [38] C. Wang, J. Gao, L. Li, and H.W. Shen. A multiresolution volume rendering framework for large-scale time-varying data visualization. In *International Workshop on Volume Graphics*, pages 11–19, 2005.
- [39] H.W. Shen, L.J. Chiang, and K.L. Ma. Time-varying volume rendering using a time-space partitioning tree. In *IEEE Visualization 99*, pages 371–377, 1999.
- [40] A. Kaufman. *Volume Visualization*. IEEE CS Press, Los Alamitos, CA, 1990.
- [41] R. Crawfis and N. Max. Direct volume visualization of three-dimensional vector fields. In *Proceedings of 1992 Workshop on Volume Visualization*, pages 55–60. IEEE Computer Society Press, Los Alamitos, CA, 1992.

- [42] P.G. Swann and S.K. Semwal. Volume rendering of flow-visualization point data. In *Proceedings of Visualization '91*, pages 25–32. IEEE Computer Society Press, Los Alamitos, CA, 1991.
- [43] W. H. Press, S. A. Teukolsky, W. T. Vetterling, and B. P. Flannery. *Numerical Recipes, 2nd Edition*. Cambridge, Cambridge, 1992.
- [44] G. Turk and D. Banks. Image-guided streamline placement. *Computer Graphics (SIGGRAPH)*, pages 453–460, 1996.
- [45] B. Jobard and W. Lefer. Creating evenly-spaced streamlines of arbitrary density. In *Proceedings of the Eurographics Workshop on Visualization in Scientific Computing*, pages 45–55, 1997.
- [46] Vivek Verma, David Kao, and Alex Pang. A flow-guided streamline seeding strategy. In *VISUALIZATION '00: Proceedings of the 11th IEEE Visualization 2000 Conference (VIS 2000)*. IEEE Computer Society, 2000.
- [47] A. Mebarki, P. Alliez, and O. Devillers. Farthest point seeding for efficient placement of streamlines. In *Proceedings of IEEE Visualization 2005*, pages 479–486, October 2005.
- [48] X. Ye, D. Kao, and A. Pang. Strategy for seeding 3d streamlines. In IEEE Computer Society Press, editor, *IEEE Visualization Proceedings 2005*, pages 471–478, October 2005.
- [49] F. B. Sachse and B. Taccardi. Visualization of electrical current flow with a new streamline technique: Application in mono- and bidomain simulations of cardiac tissue. In *Proc. 26th Conf. IEEE EMBS*, 2004.
- [50] E. Hughes, B. Taccardi, and F.B. Sachse. A heuristic streamline placement technique for visualization of electrical current flow. *J. Flow Visualization and Image Processing*, to appear, 2006.
- [51] D. C. Banks. Illumination in diverse codimensions. In *SIGGRAPH 94 Proceedings*, volume 28, pages 327–334, 1994.
- [52] M. Zöckeler, D. Stalling, and H-C. Hege. Interactive visualization of 3D-vector fields using illuminated streamlines. In *IEEE Visualization 96 Proceedings*, pages 107–113, 1996.
- [53] O. Mallo, R. Peikert, C. Sigg, and F. Saldo. Illuminated streamlines revisited. In *Proceedings of IEEE Visualization 2005*, pages 19–26, October 2005.
- [54] G. Li, U.D. Bordoloi, and H. Shen. Chameleon: An interactive texture-based rendering framework for visualizing three-dimensional vector fields. In *Proceedings of IEEE Visualization 2003*, page 32, Oct 2003.
- [55] J.P.M. Hultquist. Constructing stream surfaces in steady 3D vector fields. In *Proceedings of IEEE Visualization 1992*, pages 171–178, October 1992.
- [56] C. Garth, X. Tricoche, T. Salzbrunn, T. Bobach, and G. Scheuermann. Surface techniques for vortex visualization. In *Proceedings of Joint Eurographics - IEEE TCVG Symposium on Visualization*, pages 155–164, May 2004.

- [57] F. Sachse and B. Taccardi. Visualization of electrical current flow with a new streamline technique: Application in mono- and bidomain simulations of cardiac tissue. In *Proceedings of 26th IEEE EMBS*, 2004.
- [58] G. Erlebacher and D. Weiskopf. Flow textures: High-resolution flow visualization. In C.D. Hansen and C.R. Johnson, editors, *Visualization Handbook*, pages 279–294. Elsevier Academic Press, 2005.
- [59] B. Cabral and C. Leedom. Imaging vector fields using line integral convolution. In *Proceedings of SIGGRAPH 93*, pages 263–270. ACM SIGGRAPH, 1993.
- [60] H.W. Shen and D.L. Kao. A new line integral convolution algorithm for visualizing unsteady flows. *IEEE Transactions on Visualization and Computer Graphics*, 4(2), 1998.
- [61] B. Jobard, G. Erlebacher, and Y. Hussaini. Lagrangian eulerian advection of noise and dye textures for unsteady flow visualization. *IEEE Transactions on Visualization and Computer Graphics*, 8(3):211–222, 2002.
- [62] G.-S. Li, X. Tricoche, and C.D. Hansen. Gpuflc: Interactive and dense visualization of unsteady flows. In *Data Analysis 2006: Proceedings of Joint IEEE VGTC and EG Symposium on Visualization (EuroVis) 2006*, pages 29–34, may 2006.
- [63] H. Battke, D. Stalling, and H.-C. Hege. Fast line integral convolution for arbitrary surfaces in 3d. In Springer Berlin, editor, *Visualization and Mathematics*, pages 181–195, 1997.
- [64] B. Laramee, J.J. van Wijk, B. Jobard, and H. Hauser. ISA and IBFVS: Image space based visualization of flow on surfaces. *IEEE Transactions on Visualization and Computer Graphics*, 10(6):637–648, nov 2004.
- [65] D. Weiskopf and T. Ertl. A hybrid physical/device space approach for spatio-temporally coherent interactive texture advection on curved surfaces. In *Proceedings of Graphics Interface 2004*, pages 263–270, 2004.
- [66] M. S. Shephard, J. E. Flaherty, H. L. de Cougny, C. L. Bottasso, and C. Ozturan. Parallel automatic mesh generation and adaptive mesh control. In M. Papadrakakis, editor, *Solving Large Scale Problems in Mechanics: Parallel and Distributed Computer Applications*, pages 459–493. John Wiley & Sons, Ltd, Chichester, 1997.
- [67] V. Interrante and C. Grosch. Visualizing 3d flow. *IEEE Computer Graphics and Applications*, 8(4):49–53, 1998.
- [68] C. Resz-Salama, P. Hastreiter, C. Teitzel, and T. Ertl. Interactive exploration of volume line integral convolution based on 3d-texture mapping. In *Proceedings of IEEE Visualization 1999*, pages 233–240, October 1999.
- [69] A. Sanderson, C.R. Johnson, and M. Kirby. Display of vector fields using a reaction diffusion model. pages 115–122, 2004.

- [70] A.M. Turing. The chemical basis of morphogenesis. *Phil. Trans. Roy. Soc. Lond.*, B237:37–72, 1952.
- [71] P. Gray and S. K. Scott. Sustained oscillations and other exotic patterns of behaviour in isothermal reactions. *J. Phys. Chem.*, 59:22–32, 1985.
- [72] P. Gray and S. K. Scott. *Chemical Oscillations and Instability: Non-linear Chemical Kinetics*. Oxford University Press, 1990.
- [73] G. Scheuermann and X. Tricoche. Topological methods for flow visualization. In C.D. Hansen and C.R. Johnson, editors, *The Visualization Handbook*, pages 341–356. Elsevier, 2005.
- [74] X. Tricoche, G. Scheuermann, and H. Hagen. A topology simplification method for 2D vector fields. In *Proceedings of IEEE Visualization 2000*, pages 359–366, 2000.
- [75] X. Tricoche, G. Scheuermann, and H. Hagen. Continuous topology simplification of planar vector fields. In *Proceedings of IEEE Visualization 2001*, pages 159–166, October 2001.
- [76] C. Garth, X. Tricoche, and G. Scheuermann. Tracking of vector field singularities in unstructured 3D time-dependent data sets. In *Proceedings of IEEE Visualization 2004*, pages 329–226, 2004.
- [77] L.V. Corbin and A.M. Scher. The canine heart as an electrocardiographic generator. 41:58–67, 1977.
- [78] D.E. Roberts and A.M. Scher. Effect of tissue anisotropy on excitation potential fields in canine myocardium in situ. 51:342–351, 1982.
- [79] P. Colli Franzone, L. Guerri, C. Viganotti, E. Macchi, S. Baruffi, S. Spaggiari, and B. Taccardi. Potential fields generated by oblique layers modeling excitation wavefronts in the anisotropic myocardium. 51:330–346, 1982.
- [80] C.S. Henriquez, A.L. Muzikant, and C.K. Smoak. Anisotropy, fiber curvature, and bath loading effects on activation in thin and thick cardiac tissue preparations. 7:424–444, 1996.
- [81] P.J. Basser, J. Mattiello, and D. Le Bihan. Estimation of the effective self-diffusion tensor from the NMR spin-echo. *Magnetic Resonance*, pages 247–254, 1994.
- [82] M.A. Guttman, E.A. Zerhouni, and E.R. McVeigh. Analysis of cardiac function from mr images. *IEEE Computer Graphics and Applications*, 17(1):30–38, 1997.
- [83] E.A. Zerhouni, D.M. Parish, W.J. Rogers, A. Yang, and E.P. Shapiro. Human heart: Tagging with mr imaging – a method for noninvasive assessment of myocardial motion. *Radiology*, 169(1):59–63, 1988.
- [84] B. Wünsche and A.A. Young. The visualization and measurement of left ventricular deformation using finite element models. *International Journal of Visual Languages and Computing*, 14(4):299–326, 2003.

- [85] A.I. Veress, G.T. Gullberg, and J.A. Weiss. Measurement of strain in left ventricle during diastole with cine-mri and deformable image registration. *ASME Journal of Biomechanical Engineering*, page to appear, february 2006.
- [86] P.J. Basser and Pierpaoli C. Microstructural and physiological features of tissues elucidated by quantitative-diffusion-tensor MRI. *Journal Magnetic Resonance B*, 111(3):209–219, 1996.
- [87] C-F. Westin, S. Peled, H. Gubjartsson, R. Kikinis, and F. A. Jolesz. Geometrical diffusion measures for MRI from tensor basis analysis. In *Proceedings 5th Annual ISMRM*, 1997.
- [88] S. Pajevic and C. Pierpaoli. Color schemes to represent the orientation of anisotropic tissues from diffusion tensor data: Application to white matter fiber tract mapping in the human brain. *Magnetic Resonance in Medicine*, 42(3):526–540, 1999.
- [89] C.-F. Westin, S.E. Meier, H. Mamata, A. Nabavi, F.A. Jolesz, and R. Kikinis. Processing and visualization for diffusion tensor mri. *Medical Image Analysis*, 6:93–108, 2002.
- [90] G Kindlmann. Superquadric tensor glyphs. pages 147–154, May 2004.
- [91] D.H. Laidlaw, E.T. Ahrens, D. Kremers, M.J. Avalos, R.E. Jacobs, and C. Readhead. Visualizing diffusion tensor images of the mouse spinal cord. In *IEEE Visualization 98*, pages 127–134, 1998.
- [92] D.S. Tuch, T.G. Reese, M.R. Wiegell, and V.J. Wedeen. Diffusion MRI of complex neural architecture. *Neuron*, 40(5):885–895, 2003.
- [93] D.S. Tuch. Q-ball imaging. *Magnetic Resonance in Medicine*, 52:1358–1372, 2004.
- [94] P.J. Basser. Fiber-tractography via diffusion tensor MRI (DT-MRI). In *Proceedings of the 6th Annual Meeting ISMRM*, page 1226, 1998.
- [95] P.J. Basser, S. Pajevic, C. Pierpaoli, J. Duda, and A. Aldroubi. In vivo fiber tractography using DT-MRI data. *Magnetic Resonance in Medicine*, pages 625–632, 2000.
- [96] Song Zhang, Cagatay Demiralp, and David H. Laidlaw. Visualizing diffusion tensor MR images using streamtubes and streamsurfaces. *IEEE Transactions on Visualization and Computer Graphics*, 9(4):454–462, October 2003.
- [97] T. Delmarcelle and L. Hesselink. A unified framework for flow visualization. In R. S. Gallagher, editor, *Computer visualization: graphics techniques for scientific and engineering analysis*, pages 129–170. CRC Press, 1995.
- [98] D. Weinstein, G. Kindlmann, and E. Lundberg. Tensorlines: Advection-diffusion based propagation through diffusion tensor fields. In *Proceedings IEEE Visualization 1999*, pages 249–253, 1999.

- [99] L. Zhukov and A. Barr. Oriented tensor reconstruction: Tracing neural pathways from diffusion tensor mri. In *Proceedings of IEEE Visualization 2002*, pages 387–394, 2002.
- [100] L. Zhukov and A. Barr. Heart -muscle fiber reconstruction from diffusion tensor mri. In *Proceedings of IEEE Visualization 2003*, pages 597–602, 2003.
- [101] M. Hlawitschka and G. Scheuermann. Hot-lines: Tracking lines in higher-order tensor fields. In *Proceedings of IEEE Visualization 2005*, pages 27–34, October 2005.
- [102] A. Brun, H.-J. Park, H. Knutsson, and C.-F. Westin. Coloring of dt-mri fiber traces using laplacian eigenmaps. *Computer Aided Systems Theory - EUROCAST 2003*, 2809, 2003.
- [103] M. Cantani, R.J. Howard, S. Pajevic, and D.K. Jones. Virtual in vivo interactive dissection of white matter fasciculi in the human brain. *NeuroImage*, 17:77–94, 2002.
- [104] S. Wakana, H. Jiang, L.M. Nagae-Poetscher, P.C. van Zijl, and S. Mori. Fiber tract-based atlas of human white matter anatomy. *Radiology*, 230(1):77–87, 2004.
- [105] D. Akers, A. Sherbondy, R. Mackenzie, R. Dougherty, and B. Wandell. Exploration of the brain’s white matter pathways with dynamic queries. In *Proceedings of IEEE Visualization 2004*, pages 377–384, 2004.
- [106] J. Blaas, C.P. Botha, B. Peters, F.M. Vos, and F.H. Post. Fast and reproducible fiber bundle selection in dti visualization. In *Proceedings of IEEE Visualization 2005*, pages 59–64, 2005.
- [107] A. Brun, H. Knutsson, H. J. Park, M. E. Shenton, and C.-F. Westin. Clustering fiber tracts using normalized cuts. In *Seventh International Conference on Medical Image Computing and Computer-Assisted Intervention (MICCAI’04)*, Lecture Notes in Computer Science, pages 368–375, Rennes - Saint Malo, France, September 2004.
- [108] S. Zhang and D.H. Laidlaw. DTI fiber clustering and cross-subject cluster analysis. In *Proceedings of ISMRM*, 2005.
- [109] A. Wenger, D.F. Keefe, S. Zhang, and D.H. Laidlaw. Interactive volume rendering of thin thread structures within multivalued scientific datasets. *IEEE Transactions on Visualization and Computer Graphics*, 10(6):664–672, 2004.
- [110] G. L. Kindlmann and D. M. Weinstein. Hue-balls and lit-tensors for direct volume rendering of diffusion tensor fields. In *Proceedings of the IEEE Visualization 99*, pages 183–189, 1999.
- [111] G.L. Kindlmann and D.M. Weinstein. Strategies for direct volume rendering of diffusion tensor fields. *IEEE Trans. Visualization and Computer Graphics*, 6(2):124–138, 2000.

- [112] D. Stalling, M. Zöckler, and H.-C. Hege. Fast display of illuminated field lines. *IEEE Transactions on Visualization and Computer Graphics*, 3(2):118–128, 1996.
- [113] G. Kindlmann. *Visualization and Analysis of Diffusion Tensor Fields*. Ph.D. Thesis, University of Utah, 2004.
- [114] G. Kindlmann, X. Tricoche, and C.-F. Westin. Anisotropy creases delineate white matter structure in diffusion tensor mri. In *Proceedings of Medical Imaging Computing and Computer-Assisted Intervention, MICCAI '06, Lecture Notes in Computer Science 3749*, 2006.
- [115] C.R. Johnson. Top scientific visualization research problems. *IEEE Computer Graphics and Applications: Visualization Viewpoints*, 24(4):13–17, July/August 2004.
- [116] C.H. Wolters, A. Anwander, X. Tricoche, D. Weinstein, M.A. Koch, and R.S. MacLeod. Influence of tissue conductivity anisotropy on eeg/meg field and return current computation in a realistic head model: A simulation and visualization study using high-resolution finite element modeling. *NeuroImage*, December 2005.
- [117] D. Gullmar, J.R. Reichenbach, A. Anwander, T. Knosche, C.H. Wolters, M. Eiselt, and J. Haueisen. Influence of anisotropic conductivity of the white matter tissue on eeg source reconstruction - an fem simulation study. 7(1):108–110, 2005.
- [118] R.M. Kirby, H. Marmanis, and D.H. Laidlaw. Visualizing multivalued data from 2D incompressible flows using concepts from painting. In *Proceedings of the IEEE Visualization 99*, 1999.
- [119] C.R. Johnson and A.R. Sanderson. A next step: Visualizing errors and uncertainty. *IEEE Computer Graphics and Applications*, 23(5):6–10, September/October 2003.
- [120] B.N. Taylor and C.E. Kuyatt. Guidelines for expressing and evaluating the uncertainty of NIST experimental results. Technical report, NIST Technical Note 1297, 1994.
- [121] A.T. Pang, C.M. Wittenbrink, and S.K. Lodha. Approaches to uncertainty visualization. *The Visual Computer*, 13(8):370–390, November 1997.
- [122] G. Grigoryan and P. Rheingans. Probabilistic surfaces: Point based primitives to show surface uncertainty. In *IEEE Visualization '02*, pages 147–153. IEEE Press, 2002.
- [123] A.R. Sanderson, M. Kirby, C.R. Johnson, and L. Yang. Advanced reaction-diffusion models for texture synthesis. *Journal of Graphics Tools*, 11(3):47–71, 2006.
- [124] J.M. Kniss, R. Van Uitert, A. Stephens, G. Li, and T. Tasdizen. Statistically quantitative volume visualization. In *IEEE Visualization 2005*, 2005.

- [125] T. Tasdizen, S.P. Awate, R.T. Whitaker, and N. Foster. Mri tissue classification with neighborhood statistics: A nonparametric, entropy-minimizing approach. In *Proceedings of The 8th International Conference on Medical Image Computing and Computer Assisted Intervention (MICCAI)*, pages 517–525, 2005.
- [126] S.G. Parker and C.R. Johnson. SCIRun: A scientific programming environment for computational steering. In *Supercomputing '95*. IEEE Press, 1995.
- [127] C.R. Johnson and S. G. Parker. Applications in computational medicine using SCIRun: A computational steering programming environment. In H. W. Meuer, editor, *Supercomputer '95*, pages 2–19. Springer-Verlag, 1995.
- [128] 2007. SCIRun: A Scientific Computing Problem Solving Environment, Scientific Computing and Imaging Institute (SCI), Download from: <http://software.sci.utah.edu/scirun.html>.
- [129] R.S. MacLeod, C.R. Johnson, and M.A. Matheson. Visualization tools for computational electrocardiography. In *Visualization in Biomedical Computing*, pages 433–444, Bellingham, Wash., 1992. Proceedings of the SPIE #1808.
- [130] R.S. MacLeod, C.R. Johnson, and M.A. Matheson. Visualization of cardiac bioelectricity — a case study. In *Proceedings of the IEEE Visualization 92*, pages 411–418. IEEE CS Press, 1992.
- [131] R.S. MacLeod, C.R. Johnson, and M.A. Matheson. Visualizing bioelectric fields. 13(4):10–12, 1993.
- [132] R.S. MacLeod and C.R. Johnson. Map3d: Interactive scientific visualization for bioengineering data. pages 30–31. IEEE Press, 1993. <http://software.sci.utah.edu/map3d.html>.
- [133] B. Taccardi, B.B. Punske, R.L. Lux, R.S. MacLeod, P.R. Ershler, T.J. Dustman, and Y. Vyhmeister. Useful lessons from body surface potential mapping. 9:773–786, 1998.
- [134] B.P. Punske, Q. Ni, R.L. Lux, R.S. MacLeod, P.R. Ershler, T.J. Dustman, Y. Vyhmeister, and B. Taccardi. Alternative methods of excitation time determination on the epicardial surface. 2000.
- [135] B. Taccardi, B.B. Punske, R.S. MacLeod, and Q. Ni. Extracardiac effects of myocardial electrical anisotropy. *Biomed. Technik*, 46(Supp 2):216–218, 2001.
- [136] B.B. Punske, Q. Ni, R.L. Lux, R.S. MacLeod, P.R. Ershler, T.J. Dustman, M.J. Allison, and B. Taccardi. Spatial methods of epicardial activation time determination. 31:781–792, 2003.
- [137] B. Taccardi, B.B. Punske, R.S. MacLeod, and Q. Ni. Visualization, analysis and physiological interpretation of three-dimensional cardiac electric fields. pages 1366–1367. IEEE EMBS, IEEE, 2002.
- [138] F.H. Lopes da Silva. A critical review of clinical applications of topographic mapping of brain potentials. *J Clin Neurophysiol*, 7(4):535–551, 1990.

- [139] J.S. George, C.J. Aine, J.C. Mosher, D.M. Schmidt D.M. Ranken, H.A. Schlitt, C.C Wood wnd J.D. Lewine, J.A. Sanders, and J.W. Belliveau. Mapping function in the human brain with magnetoencephalography, anatomical magnetic resonance imaging, and functional magnetic resonance imaging. *J. Clin. Neurophysiol.*, 12(5):406, 1995.
- [140] F. Lopes da Silva. Functional localization of brain sources using EEG and/or MEG data: volume conductor and source models. *Magn Reson Imaging*, 22(10):1533–1538, December 2004.
- [141] J. Slack, K. Hildebrand, T. Munzner, and K. St. John. SequenceJuxtaposer: Fluid navigation for large-scale sequence comparison in context. In *Proceedings of German Conference in Bioinformatics*, pages 37–42, 2004.
- [142] J. Slack, K. Hildebrand, and T. Munzner. Partitioned rendering infrastructure for scalable accordion drawing (extended version). In *Information Visualization* 5(2), pages 137–151, 2006.
- [143] C. Bajaj, P. Djeu, V. Siddavanahalli, and A. Thane. Interactive visual exploration of large flexible multi-component molecular complexes. In *Proceedings of IEEE Visualization '04*, pages 243–250, 2004.
- [144] C. Bajaj, J. Castillon-Candas, V. Siddavanahalli, and Z. Xu. Compressed representations of macromolecular structures and properties. *Structure*, 13(3):463–471, march 2005.
- [145] C. H. Lee and A. Varshney. Representing thermal vibrations and uncertainty in molecular surfaces. In *Proceedings SPIE Conference on Visualization and Data Analysis*, January 20 - 25, 2002.
- [146] C. H. Lee and A. Varshney. Computing and displaying intermolecular negative volume for docking. In G. M. Nielson G.-P. Bonneau, T. Ertl, editor, *Scientific Visualization: The Visual Extraction of Knowledge from Data*. Springer-Verlag, ISBN 3-540-26066-8, 2005.